

20 **Abstract**

21 Extraction of sulfides from the partially molten mantle is vital to elucidate the cycling of metal
22 and sulfur elements between different geochemical circles but has not been investigated
23 systematically. Using laboratory experiments and theoretical calculations, this study documents
24 systematical variations in lithologies and compositions of silicate minerals and melts, which are
25 approximately consistent with the results of the thermodynamically-constrained model. During a
26 melt-peridotite reaction, the dissolution of olivine and precipitation of new orthopyroxene
27 generate an orthopyroxene-rich layer between the melt source and peridotite. With increasing
28 reaction degree, more melt is infiltrated into and reacts with upper peridotite, which potentially
29 enhances the concomitant upward transport of dense sulfide droplets. Theoretical analyses
30 suggest an energetically focused melt flow with a high velocity ($\sim 170.9 \mu\text{m/h}$) around sulfide
31 droplets through the pore throat. In this energetic melt flow, we, for the first time, observed the
32 mechanical coalescence of sulfide droplets, and the associated drag force was likely driving
33 upward entrainment of fine μm -scale sulfide. For coarse sulfide droplets whose sizes are larger
34 than the pore throat in the peridotite, their entrainment through narrow constrictions in crystal
35 framework seems to be physically possible only when high-degree melt-peridotite reaction
36 drives high porosity of peridotite and channelized melt flows with extremely high velocity.
37 Hence, the melt-rock reaction could drive and enhance upward entrainment of μm - to mm-scale
38 sulfide in the partially molten mantle, potentially contributing to the fertilization of the sub-
39 continental lithospheric mantle and the endowment of metal-bearing sulfide for the formation of
40 magmatic sulfide deposits.

41 **Plain Language Summary**

42 Sulfides are a pivotal potential reservoir for sulfur and economically important metals. Their
43 transport in the Earth's mantle plays a vital role in understanding many crucial geological and
44 environmental processes, especially the formation of mineral deposits, and the environmental
45 damage and health hazards related to volcanic eruptions. This work proposes a new driving force
46 for the upward transport of dense sulfide drops in the upper mantle that experiences partial
47 melting. The reaction between melt and rock potentially leads to focused melt flow in new-
48 forming channels with three orders of magnitude higher velocity than that of melt flowing among
49 the crystal framework of peridotite. This energetic melt flow drives the upward transport of tiny

50 μm -scale sulfide droplets in peridotite and may also facilitate the amalgamation of droplets
51 contacting each other. Coarse sulfide droplets could be possibly entrained upward through
52 narrow pore throats, especially when a high-degree melt-peridotite reaction drives fast-flowing
53 melt in the mantle with high porosity.

54 **1 Introduction**

55 Sulfide is a ubiquitous phase in the mantle (Alard et al., 2011) and an important
56 repository for sulfur and geochemically and economically important chalcophile metals, which
57 plays a pivotal role in the partitioning behaviors of PGE, Cu, and Ni (Mungall & Brenan, 2014;
58 Patten et al., 2013). Understanding the factors that control the fate of sulfide phases in the
59 partially molten mantle is of fundamental importance in exploring the recycling of sulfur and
60 chalcophile elements among different geochemical reservoirs (Ding & Dasgupta, 2017; Farquhar
61 et al., 2002; Yao et al., 2018; Chen et al., 2022) and identifying the re-fertilization of the
62 depleted lithospheric mantle, which potentially provides the metal endowment for the formation
63 of Cu-rich porphyry and/or Ni-rich magmatic ore system (Holwell et al., 2022; Lee & Tang,
64 2020; Mungall et al., 2015; Zhao et al., 2022). However, it remains highly contentious for the
65 driving forces of the transport of metal-bearing sulfide liquid, which severely blocks our
66 understanding of the details of fertilization processes that occurred in the sources of sulfide-
67 related magmatic and hydrothermal deposits.

68 Conventionally, the removal of sulfide from a partially molten peridotite requires
69 progressive dissolution of sulfide into the departing silicate melt (Holzheid & Grove, 2002;
70 Mungall & Brenan, 2014; Yao et al., 2018). Nevertheless, the mechanical entrainment of sulfide
71 could also potentially be an efficient process driving the redistribution and local enrichment of
72 sulfur and chalcophile elements in the mantle (Iacono-Marziano et al., 2022; Heinrich &
73 Connolly, 2022; Z. Wang et al., 2020; Yao & Mungall, 2020). Although a small amount ($<$
74 percolation thresholds) of sulfide under hydrostatic conditions may not be entrained through the
75 slow porous flow of silicate melt due to high surface tension (Bagdassarov et al., 2009; Holzheid
76 et al., 2000; Yoshino et al., 2003, 2004), it has been argued that the extraction of sulfide driven
77 by stress in a partially molten peridotite could be further facilitated by the directional porous
78 flow of silicate melt, strongly affecting the fractionation and abundances of chalcophile metals in
79 the mantle melting products, *i.e.*, basalts (Ballhaus et al., 2006; Bockrath et al., 2004; Z. Wang et

80 al., 2020). Except for the deviatoric stress, a preliminary experimental study (Wang & Jin, 2020)
81 proposed that during the melt-rock reaction, entrainment of sulfide liquid may be enhanced by
82 the reaction infiltration instability (RII) in the partially molten peridotite when a reacting melt
83 percolates through a dissolvable, porous, melt-mineral mixture. The mechanical transport and
84 enrichment of sulfide during this melt-rock reaction have been extensively demonstrated in
85 mantle peridotites, which has clarified some geochemical paradoxes of the
86 chalcophile/siderophile elements (Ciazela et al., 2018; Lorand & Luguet, 2016). The RII theory
87 proposed by Chadam et al. (1986) also applies to magmatic systems by introducing compaction
88 of crystal mush and driving a solubility gradient along the flow direction instead of the
89 propagating reaction front (Aharonov, 1995), resulting in positive feedback among the increasing
90 permeability driven by melt-rock reaction and the associated reinforcement of melt flux in
91 reacting regions. This melt-rock reaction is well known as a pervasive process even forming
92 melt-rich channels with an extremely speedy magma flow due to the positive feedback in
93 partially molten regions of the mantle, which has been broadly demonstrated by geological
94 investigations (e.g., Kelemen et al., 1995; Sundberg et al., 2010), high-temperature, high-
95 pressure (HTHP) laboratory works (e.g., Daines & Kohlstedt, 1994; Pec et al., 2015) and
96 theoretical analyses (Aharonov, 1995; Chadam et al., 1986; Spiegelman et al., 2001). During a
97 reaction of melt with a depleted mantle, melt re-fertilization processes potentially occur, thereby
98 impregnating the mantle with sulfides, which have been widely found in mantle xenoliths,
99 orogenic and abyssal peridotites (e.g., Ciazela et al., 2018; Luguet et al., 2003; Niu, 2004; Wang
100 et al., 2009).

101 Although it has been tentatively demonstrated that the rapid enough ascending magma
102 flow in these melt-rich channels could hold upward entrainment of large olivine phenocrysts or
103 even dense sulfide droplets during a melt-rock reaction (Pec et al., 2017; Wang & Jin, 2020),
104 extraction of sulfide driven by the RII has received little attention, and the precise physical and
105 chemical constraints about these processes appear to be worth studying thoroughly. Here we
106 conducted systematically two-layer reaction experimental studies in which a partially molten
107 peridotite was placed on a sulfide-bearing silicate melt source to explore the entrainment of
108 sulfide liquids driven by the RII and trace the physical and chemical variations of liquid and
109 solid phases during these processes, which sheds lights on the fertilization of lithospheric mantle,
110 as well as the formations of magmatic and/or hydrothermal sulfide deposits.

111 **2 Experimental Methods**

112 2.1 Starting materials

113 As a melt source, the starting materials were a mixture of the powdered calc-alkaline
114 tholeiitic basalt (70 wt.%) from the East Pacific Rise (102.7044 °W, 2.64961 °S), olivine crystals
115 (20 wt.%) from fresh spinel lherzolite xenoliths at Damaping (Hannuoba region, North China),
116 and sulfide aggregates (10 wt.%) from Jinchuan Ni-Cu sulfide deposit, NW China. Additionally,
117 0 or 2 wt.% oceanic sediments (mainly carbonate) were mixed into the melt source. The sulfide
118 aggregate (59 wt.% pyrrhotite, 36 wt.% pentlandite, and 5 wt.% chalcopyrite) adopted here is
119 similar to that in massif peridotites (Lorand et al., 2010), and was grounded in alcohol for about
120 6h to < 10 μm measured by using the scanning electron microscope (SEM).

121 To prepare a partially molten rock, the olivine and clinopyroxene crystals from
122 Damaping spinel lherzolite xenoliths were mixed in a 50:50 ratio by weight. Then, ~ 0 or ~ 5
123 wt.% calc-alkaline tholeiitic basalt was added to change the initial porosity of the crystal
124 framework. All silicate mineral grains were ground to about 10-20 μm grain size in an agate
125 mortar. The partially molten rock was placed on the melt source to explore the possible upward
126 transport of dense sulfides from the melt source to the peridotite. The length ratio of these two
127 parts was slightly larger than ~ 1:1 to avoid chemical equilibration among them over the
128 experimental time scales. Compositions of these starting materials were described by Z. Wang et
129 al. (2020) (Table S3), and Table 1 lists the experimental conditions.

130 2.2 Experimental methods and analytical techniques

131 The two-layer reaction experiments were conducted via a 150 Ton non-end-loaded type
132 piston-cylinder press at China University of Geosciences. Starting materials mentioned above are
133 loaded into a cylindrical platinum (Pt) capsule (3.75 mm diameter; 5-6 mm high) with a graphite
134 inner sleeve (Figure 1-inset in the lower left). Due to the graphite inner sleeve, the oxygen
135 fugacity of this experimental system was maintained at about CCO-0.8 (the graphite-CO₂
136 buffer), which corresponds to a log fO_2 < FMQ-2 log unit at ~ 1,360 °C and 1.5 GPa (e.g.,
137 Médard et al., 2008). Information on experimental assembly can be found in our previous work
138 (Z. Wang et al. 2020). In order to remove absorbed water, a 12-hour heating (120 °C) in a
139 vacuum oven is conducted for all capsules before being sealed, and we did not observe any

140 apparent sulfur loss during this drying. The experiment conditions in Table 1 should be held for
141 12-72 h, and then these materials were quenched to room temperature.

142 Polished sections were prepared from the recovered experimental specimens cut parallel
143 to the specimen axis. The observation of microstructure in these sections was conducted via a
144 Quanta 450 field-emission scanning electron microscope (FE-SEM) at China University of
145 Geosciences, with a 6.0 μm spot size, 20 kV accelerating voltage, and 12 mm working distance.
146 The backscattered electron (BSE) images were adopted to measure the morphological
147 characteristics of experimental products, such as the dissolution distance, the thickness of
148 reactive boundary layers, and the size of sulfide droplets. Quantitative compositional analyses for
149 olivine and clinopyroxene were obtained via a JEOL JXA-8230 electron probe microanalyzer
150 with four wavelength-dispersive spectrometers (WDS) at China University of Geosciences, with
151 an accelerating voltage of 15 kV, a probe current of 20 nA and a beam diameter of 1 μm .
152 Sulfides were analyzed with a higher accelerating voltage (20 kV), and the compositions of
153 quenched silicate melts were measured with a smaller probe current (10 nA). A defocused beam
154 of 20-30 μm diameter was adopted here for all the standardizations, quenched melts, and
155 sulfides. Dwell times were 10s on element peaks and half that on background locations adjacent
156 to peaks. Raw X-ray intensities were corrected using a ZAF (atomic number, absorption,
157 fluorescence) correction procedure. A series of natural and synthetic SPI standards were utilized
158 and changed based on the analyzing minerals. The following standards were used: sanidine (for
159 K), pyrope garnet (for Al), almandine garnet (for Fe), diopside (for Ca, Si, Mg), jadeite (for Na),
160 rhodonite (for Mn), olivine (for Si, Mg), rutile (for Ti), apatite (for P), chromium oxide (for Cr).
161 The analytical standards for sulfides were pentlandite (for Fe, Ni, S) and native copper (for Cu)
162 (Pan et al., 2023).

163 **3 Results**

164 In order to investigate the physical migration of sulfide during reaction infiltration of
165 silicate melt in the partially molten mantle, we have conducted eight reaction experiments at 0.5-
166 1.5 GPa, 800-1,300 $^{\circ}\text{C}$, and 12-72 h (Table 1). Generally, several distinct lithological regions
167 were developed and, from bottom to top, respectively separated by a diffuse-dominated,
168 mineralogical interface in these two-layer reaction experiments (Figure 1; Figures S2-S8). The

169 freeware ImageJ (<http://imagej.nih.gov/ij/>) from the National Institute of Health was adopted to
170 analyze all two-dimensional BSE images obtained here.

171 3.1 Phase assemblages and textures

172 Under the low-temperature, high-pressure conditions (800 °C and 1.5 GPa), both
173 minerals and sulfides were generally polygonal and not molten, and sulfide droplets in the lower
174 part of the sample were uniformly distributed in pores among silicate grains. At 1.5 GPa, when
175 the experimental temperatures exceed ~1,250 °C, the basaltic material was completely molten,
176 and the diameter of sulfide droplets ranges from several μm to $> 100 \mu\text{m}$ (Figure 1).
177 Gravitational segregation of sulfide was insignificantly observed in all sections, but obviously,
178 some huge sulfide droplets were attached to the wall of the graphite capsule, especially at high
179 temperature and long experiment durations (Figure 1). These coarse droplets were excluded from
180 the collected data to calculate the average sulfide size. Tiny exsolution lamellae with higher
181 backscattered electron (BSE) intensity were occasionally observed in some quenched large
182 sulfide droplets. Sometimes silicate melts were pooled at the edge of the sample (Figure 1).

183 In all high-pressure experiments (1.5 GPa), an orthopyroxene (Opx)-rich reaction layer
184 (ORL) was formed at the boundary of the lower melt source and upper partially molten peridotite
185 due to the reaction between them, and chiefly composed of Opx grains, silicate melt, and sulfide
186 droplets (Figure 1). With increasing the annealing time and/or run temperature, the morphology
187 of ORLs became more irregular (Figure 1b; Figures 2a, b, and d), and small olivine inclusions
188 were observed in a few large Opx grains (Figure 2a). The ORL at 1,300°C was even ruptured
189 mainly due to the growth of several Opx grains to enormous size ($> 100 \mu\text{m}$) and possible
190 gravitational settling (Figure 2d). We also observed the bulge of ORL toward the melt source
191 (Figure 1b), which can be attributed to the slight gravitational settling of Opx and volumetric
192 shrinkage of the melt source after the upward reactive percolation of silicate melt. Thus, the
193 original interface between the melt source and peridotite before the experimental reaction cannot
194 be marked by the offset of the graphite inner sleeve. At 1,250 °C, the thickness of ORL increases
195 from $\sim 118 \pm 11 \mu\text{m}$ (1σ) at 12 h to $\sim 416 \pm 119 \mu\text{m}$ at 72 h, which is likely a linear function of
196 the square root of the run duration (slope = 0.78 ± 0.05) (Figure 3a-blue line). With increasing
197 the temperature to 1,300 °C, the thickness increases considerably to $500 \pm 128 \mu\text{m}$ at 12 h
198 (Figure 3a), implying the contribution of a higher temperature to the growth of ORL.

199 Additionally, based on the linear fit, the addition of 5 wt.% basalts into the partially molten
200 peridotite (run PC548) or 2 wt.% oceanic sedimentary into the melt source (run PC560) seems to
201 have no significant effect on the thickness of ORL (Figure 3a).

202 On the other hand, peridotites in the upper part of our samples were in disequilibrium
203 with silicate melt at these run conditions, thereby should be dissolved essentially into the melt.
204 The degree of dissolution is indirectly quantified via the dissolution distance (Figure 3b), which
205 is the distance between the current boundary (Figure 1-blue dotted lines) and the original
206 interface (Figure 1-red dotted lines) that is approximately represented by a sharp decrease in the
207 size of sulfide droplets in the melt source. All these dissolution distances are measured at least 5
208 times around the central part of experimental charges. Similarly, dissolution distance linearly
209 increases with the square root of time (Figure 3b-blue line) at 1,250 °C, and the increase of
210 temperature to 1,300 °C significantly enlarges the dissolution distance (Figure 3b). The addition
211 of oceanic sedimentary (PC560) or basalt (PC548) has no substantial effect on the dissolution
212 distance (Figure 3b).

213 Moreover, based on analyses of SEM images, with increasing run duration or
214 temperature, more silicate melt penetrated the Opx reaction layer into the partially molten
215 peridotite ($\sim 4.65 \pm 0.78$ area% at 12 h; $\sim 7.13 \pm 0.58$ area% at 72 h) (Figure 4a), resulting in the
216 formations of melt junctions and channels among silicate minerals, and even some large melt
217 pools just above the ORL (Figure 2c; Figures S2-S8). At 1.5 GPa, with increasing annealing time
218 from 12 h to 72 h, the grain size of silicate minerals increases from 8.1 ± 3.4 μm to 11.0 ± 4.9
219 μm in the partially molten peridotite (Figure 4b; Supporting information; Table S1). Under
220 conditions of high temperature (1,300 °C) and long-run duration (72 h), an olivine-melt layer,
221 consisting of sulfide, olivine, and silicate melt, is present above the ORL (Figures 2a and 2d,
222 Figures S3 and S5), which may be attributed to the dissolution of clinopyroxene and
223 reprecipitation of olivine during the melt-peridotite reaction. Additionally, crystal faces between
224 olivine grains were open and full of silicate melt, forming abundant melt channels among the
225 crystal framework (Figure 2c, Figures S2-S8).

226 In the melt source, an amount of Opx grains were produced by the reaction between
227 olivine in starting materials and convecting silicate melt (Figure 1), and there is commonly no
228 significant boundary between these Opx grains and the ORL. The mean area-weighted diameter

229 of sulfide droplets was $\sim 4.1 \pm 0.1 \mu\text{m}$ in a low-temperature hot-press experiment (PC537, 800
230 $^{\circ}\text{C}$), which potentially denotes the initial size of sulfide droplets in the starting material. At a
231 higher temperature (1,250 $^{\circ}\text{C}$), sulfide size increases from $\sim 14.7 \pm 0.2 \mu\text{m}$ to $\sim 49.4 \pm 1.6 \mu\text{m}$
232 with increasing the annealing time from 12 h to 72 h (Figure 5a; Table S2), in which the larger
233 standard deviations from the long annealing time (72 h) experiments may be partly attributed to
234 the presence of some enormous ($> 50 \mu\text{m}$) and tiny ($< 1 \mu\text{m}$) sulfide droplets. Under the same
235 annealing time (48 h), there is no conspicuous increase in sulfide size when 5 wt.% basalt was
236 added to the peridotite (PC548), but a slight increase in sulfide size was observed if the
237 experimental temperature increased to 1,300 $^{\circ}\text{C}$ (PC527) (Figure 5a). The addition of carbonate
238 into the melt source (PC560) resulted in a significant increase in sulfide size to $\sim 54.0 \pm 1.6 \mu\text{m}$
239 at 24 h (Figure 5a). Additionally, we also observed that the number density of sulfide droplets
240 uniformly decreases with increasing annealing time in the lower melt source (Figure 5a-inset).
241 The area fraction of sulfide in the melt source of the low-temperature experiment (800 $^{\circ}\text{C}$) was \sim
242 $3.26 \pm 0.12 \text{ area}\%$. At 1,250 $^{\circ}\text{C}$, the area fraction was essentially constant ($3.44 \pm 0.14 \text{ area}\%$ at
243 12h; $3.50 \pm 0.15 \text{ area}\%$ at 48h) when the annealing time was less than 48 h, but a visible increase
244 ($5.46 \pm 0.22 \text{ area}\%$) can be observed for a longer annealing time, 72 h (Figure 5b). A similar
245 trend was also shown in the upper part of samples (Figures 5c and 5d), which may be due to
246 more silicate melts infiltrating into the upper part of samples with increasing annealing time to
247 72 h (Figure 4). As previously observed (Yoshino & Watson, 2005), the diffusion of Fe and Ni
248 components from silicate phases into sulfide liquids may be one of the reasons for the increase of
249 sulfide area fraction in the melt source. In contrast, with increasing temperature to 1,300 $^{\circ}\text{C}$, a
250 lower area fraction ($2.93 \pm 0.07 \text{ area}\%$) of sulfide was observed even in the experiment with a
251 short annealing time (12 h) (Figure 5b), potentially due to partial dissolution of sulfide driven by
252 the higher sulfur content at sulfide saturation (SCSS) at high temperature (*e.g.*, Liu et al., 2007;
253 Mavrogenes & O'Neill, 1999). Similarly, the additions of basalt and carbonate enhance the
254 permeation of more silicate melt into the upper part of samples, thereby increasing the area
255 fraction of sulfide in the melt source (Figure 5b).

256 Based on the SEM images of products from these high-temperature experiments (1,250
257 $^{\circ}\text{C}$), it becomes evident that sulfide droplets in the melt source were entrained into the partially
258 molten peridotite by a porous flow of silicate melt during the melt-peridotite reaction (Figure 2).
259 With permeating more silicate melt upwards, more and larger sulfide droplets can be observed in

260 the partially molten peridotite, and meanwhile their sizes (area-weighted diameter $\sim 3.1 \pm 0.1 \mu\text{m}$
261 at 12 h to $\sim 11.1 \pm 0.4 \mu\text{m}$ at 72 h) and area fractions ($\sim 0.15 \pm 0.05 \text{ area}\%$ at 12 h to $\sim 0.49 \pm$
262 $0.03 \text{ area}\%$ at 72 h) increase with the increasing annealing time at 1,250 °C (Figures 5c and 5d;
263 Table S2). Apparently, the addition of carbonate and 5 wt.% basalt into melt source and partially
264 molten peridotite, respectively, drives a higher area fraction and larger size of sulfide droplet in
265 the upper part of samples (Figures 5c and 5d). Hence, these observations propose that the ORL
266 may not efficiently prevents the upward transport of silicate melt and sulfide droplets from the
267 lower melt source to the upper molten peridotite.

268 Notably, under the condition of lower pressure (0.5 GPa), some vapor bubbles have been
269 found in the partially molten peridotite due to the exsolution of volatile (mainly H₂O) in the
270 starting basaltic material, and they mostly absorb on sulfide droplets to form compound drops,
271 which has been proposed to potentially enhance the upward transport of sulfide (Figure S7;
272 Mungall et al., 2015; Yao & Mungall, 2020).

273 3.2 Phase compositions

274 3.2.1 Mineral compositions

275 Figure 6 and Figure 7 respectively showed the compositional variations of olivine and
276 clinopyroxene as a function of distance away from the final melt-peridotite interface (Table S4).
277 At 1.5 GPa and 1,250-1,300 °C, from the far-field region to the interface, olivine grains became
278 gradually lower in the Mg# (defined as molar $\text{Mg}/(\text{Mg}+\text{Fe}) \times 100$) and concentrations of SiO₂,
279 MgO, and NiO, and meanwhile shown the increases in the FeO and MnO contents (Figure 6).
280 Compared with the low-temperature, hot-press experiment (PC537) (Figure 6 purple dotted
281 lines), olivine grains from high-temperature experiments contain lower MgO and NiO, and
282 higher FeO and CaO concentrations. By contrast, olivine compositions in experiments PC548 (5
283 wt.% basalts) and PC559 (0.5 GPa) were roughly constant across the partially molten peridotite,
284 whereas olivine grains crystallized in the melt source at lower-pressure experiment (0.5 GPa,
285 PC559) had lower Mg#, MgO, SiO₂ and higher FeO than those in the peridotite region (Figure
286 6).

287 In contrast to olivine, more scatter compositions were observed in the clinopyroxene
288 (Cpx) grains from the partially molten peridotite (Figure 7). Only near the melt-rock interface,

289 the trends of decreasing Mg# and CaO and increasing FeO were present in Cpx grains from all
290 high-pressure experiments, whereas the Cpx compositions in the low-pressure and carbonate-
291 bearing experiment (PC559 and PC560) were essentially constant across the peridotite region
292 (Figure 7). On the other hand, the Opx grains in the reaction layer and melt source were the
293 products of silicate melt-olivine reaction. No distinct compositional difference was observed in
294 these Opx grains (Figure S9; Table S4).

295 3.2.2 Silicate melt and sulfide liquid compositions

296 The variations of the reacted melt compositions in these experiments mostly depend on
297 the extent of the melt-rock reaction and the formation of a new major phase. In the melt source,
298 with increasing run time and/or temperature, the compositions of silicate melt became higher in
299 CaO and MgO concentrations, and lower in SiO₂, Al₂O₃, and FeO (Figure 8; Table S5), implying
300 the effect of high-degree melt-peridotite reaction on the melt composition. No distinct variation
301 of the melt sulfur contents was observed under the conditions of 1,250 °C and 1.5 GPa. Based on
302 two new SCSS models (Chowdhury and Dasgupta, 2020; Smythe et al., 2017), the calculated
303 ranges of SCSS in silicate melt are almost the same or slightly lower than our results within the
304 error of measurement (Figure 8f-shadow gray region), potentially indicative of sulfur-saturated
305 silicate melt in these experiments. Moreover, the calculated SCSS in the melt source is nearly the
306 same as those in the interface within the error, which is consistent with our measurements
307 (Figure 8f). The decreases in pressure and temperature respectively to 0.5 GPa and 1,200 °C
308 caused the obvious increases in SiO₂ and Al₂O₃ concentrations and decreases in MgO and S
309 concentrations in silicate melt (Figures 8a, 8b, 8e, and 8f). No significant variations of melt
310 compositions were observed between the melt source and melt-peridotite interface within the
311 error of measurement (Figure 8), suggesting the convective flow is strong enough to drive the
312 chemical equilibrium of silicate melt. The composition of primary silicate melt infiltrating into
313 the peridotite cannot be analyzed due to the small scale. In addition, $\sim 1.57 \pm 0.15$ wt.% H₂O was
314 detected in the reacted melts from experiments PC520 and PC528 using the Fourier Transform
315 Infrared Microscopy (Supporting Information, Mercier et al., 2010), which is slightly higher than
316 that of basalt (~ 1.19 wt.%) added in the starting materials. On the basis of these melt
317 compositions, the viscosity (μ_m) of the starting basalt (~ 1.19 wt.% H₂O) before the melt-rock
318 reaction can be calculated as ~ 10.8 Pa·s at 1.5 GPa and 1,250 °C by using the model from
319 Giordano et al. (2008), whereas the μ_m of reacting melt after the reaction decreases to ~ 1.2 -2.7

320 Pa·s at 1.5 GPa and 1,250-1,300 °C assuming the water content of ~ 1.5 wt.% (Figure 8g). When
321 the pressure and temperature respectively decrease to 0.5 GPa and 1,200 °C, the reacting melt
322 has a higher viscosity of ~10.5 Pa·s. Additionally, there is no evident difference in melt viscosity
323 between the melt source and the melt-peridotite interface. However, the addition of carbonate
324 (PC560) potentially leads to a peculiarly lower melt viscosity (~ 0.25 Pa·s) estimated by using a
325 simple model (Di Genova et al., 2014) under the assumption of the 2 wt.% carbonate dissolved
326 in silicate melt, which represents an order-of-magnitude evaluation of the melt viscosity due to
327 the uncertainty of extrapolation (Figure 8g).

328 Except for several large sulfide droplets containing the Ni-rich quenched phases, the
329 composition of sulfide was homogeneous in the lower melt source of all experiments. In the 12 h
330 experiment, the S content, Ni/S and Fe/S ratios of sulfide liquid were ~ 35.16 ± 0.72 wt.%, ~
331 0.39 ± 0.03, and ~ 1.43 ± 0.04, respectively, and these values remained constant within the error
332 of measurement when the annealing time increases to 72 h (S ~ 35.74 ± 0.74 wt.%, Ni/S ~ 0.37 ±
333 0.09, Fe/S ~ 1.42 ± 0.06). However, the Cu/S ratio of sulfide liquid slightly decreased from
334 0.017 ± 0.004 at the 12 h to 0.009 ± 0.002 at the 72 h at 1,250 °C, while an obvious increase in
335 the Cu/S ratio (~ 0.046 ± 0.010) was observed at 1,300 °C (Table S4).

336 **4 Discussion**

337 **4.1 Grain-scale processes in melt-peridotite reaction**

338 Firstly, if the upper peridotite reaches equilibrium at 1.5 GPa and 1,250-1,300 °C, the
339 corresponding melt fraction will be less than 0.04-0.08 wt.% based on the thermodynamic model
340 via the pMELTS (Ghiorso et al., 2002), implying that the self-partial melting of peridotite at the
341 experimental conditions is negligible here. The observed variations of melt area fraction, phase
342 proportions, and minerals' sizes and compositions in our experiments can be primarily attributed
343 to the melt-peridotite reaction. On the other hand, the upper peridotites are not in equilibrium
344 with the starting melts at the experimental conditions, and hence olivine and clinopyroxene in the
345 peridotite part should partially or completely dissolve in the reacting and upward percolating
346 melt (Liang, 1999; C. Wang et al., 2020). In multicomponent partially molten systems, the melt-
347 peridotite reaction is suggested to occur via multi-scale mass transfer processes that inevitably

348 involve both the grain-scale dissolution-precipitation-reprecipitation and diffusion, in
 349 conjunction with large-scale advective transport (Cascio et al., 2008; Morgan & Liang, 2005).

350 In our high-temperature, high-pressure experiments (1.5 GPa and 1,250-1,300 °C) here,
 351 due to the disequilibrium between melt and peridotite, the consequent grain-scale processes can
 352 mostly occur via the dissolution, precipitation, and reprecipitation of mineral grains, which is
 353 evident from the formation of ORL. In the lower melt source, the basaltic melt in starting
 354 materials is olivine-undersaturated, and thus the melt-rock reaction between basaltic melt and
 355 olivine produces new Opx grains (Figure 1), which is consistent with the following reaction:



358 where subscripts 0 and 1 designate melt and mineral grains from starting materials and the
 359 reaction products, respectively. This reaction should occur via the dissolution of olivine, and
 360 precipitation of new orthopyroxene, largely contributing to the formation of ORL in the interface
 361 between the peridotite and melt source (Figure 1a). It is well known that dissolution and
 362 precipitation occur simultaneously during the development of the ORL under high pressure (> 1
 363 GPa) (Cascio et al., 2008; Morgan & Liang, 2003). With increasing the degree of melt-peridotite
 364 reaction (a longer run duration and/or higher temperature), an olivine-melt layer above the ORL
 365 is formed by the further dissolution of olivine and few clinopyroxene grains, with concomitant
 366 reprecipitation of fresh olivine grains in the melt reaction flow (Figure 2) (Kelemen et al., 1995).

367 The grain size of silicate minerals plays a vital role in affecting the physical properties of
 368 upper partially molten peridotite, such as permeability (Faul, 2001). Here, the growth of silicate
 369 mineral sizes in the upper partially molten peridotite with increasing annealing time (Figure 4b)
 370 is mostly driven by a reduction of grain boundary energy (Faul & Scott, 2006) and demonstrates
 371 that textural coarsening by which small-size crystals are consumed to support the growth of
 372 coarser grains (Higgins, 1998, 2011; Yao et al., 2017), may outweigh the decreasing-size effect
 373 related to reprecipitation of new, fine-grained crystals. The transference of material from
 374 dissolved olivine to other grains occurs via diffusion through grain boundaries, crystals
 375 themselves, and interstitial melt (Yao et al., 2017), while the last one is much faster and becomes
 376 the main pathway of these grain-scales processes. Finally, large-scale advective transport of

377 reacting melt is evident from the variations of melt area fraction in the partially molten peridotite
378 and the formations of melt junctions and channels (Figure 1; Figure 4a).

379 Based on the parabolic law of diffusive dissolution (Liang, 1999; Zhang et al., 1989), the
380 slope (*i.e.*, the diffusive dissolution constant) of the fitted linear regression line for our
381 experiments is used to estimate the growth rate of ORL (k_{ORL}), which is about $\sim 0.78 \pm 0.05$
382 $\mu\text{m}/\text{s}^{0.5}$ at 1.5 GPa and 1,250 °C. This growth rate is far lower than those of some previous
383 experiments conducted at higher temperatures and/or pressures (Figure 3a) (Morgan & Liang,
384 2005; C. Wang et al., 2020). The thickness of ORL in experiment PC527 at 1.5 GPa and a higher
385 temperature ($\sim 1,300$ °C) has a faster-increasing tendency ($k_{ORL} = 2.37 \pm 0.14 \mu\text{m}/\text{s}^{0.5}$), consistent
386 with the experiments under 2 GPa and 1,375 °C (C. Wang et al., 2020). This tendency of ORL
387 growth is likely unchanged in the experiments with the carbonate-bearing melt source (PC560)
388 and silicate melt-bearing peridotite (PC548) (Figure 3a), implying an insignificant effect of melt
389 composition and porosity on the growth of ORL. Our results indicate that the increase in
390 temperature will potentially enhance the growth rate of ORL thickness during the melt-rock
391 reaction, which can be mostly attributed to the higher diffusivities of elements in silicate melts at
392 a higher temperature (Mungall, 2002; Zhang et al., 2010).

393 Similarly, we observed the linear increase of dissolution distance with the square root of
394 time (Figure 3b), suggesting that a substantial amount of peridotite was dissolved in the
395 percolating melt. At 1.5 GPa and 1,250 °C, the dissolution rate of peridotite evaluated by the
396 slope of the linear regression line ($k_{diss} = 0.58 \pm 0.08 \mu\text{m}/\text{s}^{0.5}$) is lower than those in previous
397 experiments with higher temperatures and pressures (Figure 3b, C. Wang et al., 2013, 2020),
398 indicating that relatively high temperature also increases the dissolution rate. Moreover, the
399 higher dissolution rate of peridotite at experiment PC527 (1,300 °C) implies that an increase in
400 temperature significantly enhances melt-rock reaction (Mitchell & Grove, 2016). The high
401 content of water ($\sim 1.57 \pm 0.15$ wt.%) in silicate melt could enhance the formation of several
402 enormous Opx grains in the ORL (Figure 2) (Wang et al., 2016), partly because the addition of
403 water can strongly depress the peridotite solidus. This may be also the reason for the large
404 standard deviations of the dissolution rate in experiments PC527 and PC545 with a high
405 temperature (1,300 °C) and long annealing time (72 h). Overall, the growth rate of the ORL is
406 generally higher than the peridotite dissolution rate, which is potentially attributed to the volume-
407 increasing reaction during the replacement of olivine by orthopyroxene (Milke et al., 2009).

408 4.2 Compositional variations of melt and minerals

409 During a melt-peridotite reaction, besides the systematic changes in mineralogy and
410 texture of peridotite, we also observed the compositional variations of melt and minerals in the
411 reaction couple (Figures 6-8), which have been widely used to outline the grain-scale processes
412 governing this melt-peridotite reaction (Mallik & Dasgupta, 2012; C. Wang et al., 2020). On the
413 other hand, a thermodynamically-constrained mixing model has been recently used to examine
414 the variations of major element compositions of minerals during the melt-peridotite interaction
415 (Lambart et al., 2012; Pin et al., 2022; Shaw et al., 2018), and this forward model may offer a
416 key to testing and understanding the compositional evolution of our experimental products.

417 The melt-peridotite reaction here is modeled as a simplified, thermodynamic process in
418 which the peridotite is continually impregnated by a finite amount of basaltic melt from the
419 lower melt source, which is the same as the assumption in previous works (Lambart et al., 2012;
420 Pin et al., 2022; Shaw et al., 2018). After each increment of melt impregnation, the infiltrated
421 melt will eventually be equilibrated with surrounding peridotite, and the thermodynamic
422 properties of the whole system are adopted as a reference for the next increment. In each
423 increment, the proportions and compositions of melt and solid phases after chemical re-
424 equilibrium can be obtained by finding the minimum Gibbs energy of the whole system (Pin et
425 al., 2022; Yao et al., 2018). This process is modeled by constantly adding up to 200 g of the
426 lower basaltic melt by increments of 0.5 g, to 100 g of the upper peridotite, using the pMELTS
427 of alphaMELTS (Ghiorso et al., 2002; Ghiorso & Sack, 1995; Smith & Asimow, 2005) in
428 isenthalpic mode at 1.5 GPa, 1,250-1,300 °C and $\Delta QFM-2.0$. Here, the incremental addition of
429 basaltic melt corresponds to the increase of melt: peridotite ratio from 0.005 to 2.

430 Our simulation shows that the mass fraction of olivine decreases from ~ 49 wt.% to ~ 22
431 wt.% with the increasing melt: peridotite ratio from 0.005 to 2 (Figure 8h). The silicate melt
432 becomes saturated with orthopyroxene when the melt: peridotite ratio reaches ~ 0.22. After this
433 point, the mass fraction of new orthopyroxene precipitated from silicate melt quickly increases to
434 ~ 32 wt.% at the melt: peridotite ratio of 2 (Figure 8h). The mass fraction of clinopyroxene in
435 peridotite has a quick increase from ~ 51 wt.% to ~ 57 wt.% before the precipitation of
436 orthopyroxene, but then slowly decreases to ~ 46 wt.% at melt: peridotite ratio = 2 (Figure 8h).
437 Hence, the increase in orthopyroxene proportion is mostly due to the dissolution of olivine,

438 accompanied by a limited contribution from the consumption of less than ~ 5 wt.%
439 clinopyroxene, which approximatively coincides with the hypothetical Reaction 1 mentioned
440 above.

441 Concurrently, the melt penetrates upwards and further reacts with the peridotite to result
442 in systematic variations of the compositions of olivine and Cpx grains towards the melt-rock
443 interface (Figure 6 and Figure 7). The modeled compositional evolutions of olivine show a
444 decreasing trend of MgO content from ~ 49.3 wt.% to ~ 44.1 wt.%, an increase of FeO content
445 from ~ 9.0 to ~ 14.5 wt.%, and the associated decrease of Mg# from ~ 90.7 to ~ 84.4 , when the
446 melt: peridotite ratio increases from ~ 0.005 to ~ 1.5 (Figure 6h). In the same range of melt:
447 peridotite ratio, the clinopyroxene has an obvious increase in its MgO content (from ~ 17.5 to \sim
448 20.0 wt.%) and approximately constant Al_2O_3 content (Figure 7h). The trends of these
449 compositional variations of minerals are nearly in agreement with those of our experiments,
450 except for the low-pressure experiment (PC559, Figure 6h and Figure 7h). Therefore, the
451 measured compositional variations of olivine and clinopyroxene as a function of distance away
452 from the final melt-peridotite interface may be connected to the melt: peridotite ratio during the
453 reaction. The measured compositions of olivine and Cpx grains just above the final melt-
454 peridotite interface are approximately consistent with those results simulated thermodynamically
455 (Figures 6h and 7h-gray shadow regions) in the melt-peridotite ratio of 1.0 to 1.5, which implies
456 that they have obtained locally chemical re-equilibrium with the reacting melt that is about ~ 1.0 -
457 1.5 times the initial mass of peridotite in the same region. As the distance away from the final
458 melt-peridotite interface grows, the growing MgO and Mg# contents of olivine reflect the
459 decrease of melt: peridotite ratio, and consequently imply the gradual weakening of melt-
460 peridotite reaction. Therefore, when the upward-flowing melt encounters the partially molten
461 peridotite that initially has a low permeability, melt convection, backflow, and the associated
462 high-degree melt-peridotite reaction mostly occur at the bottom of peridotite, leading to an
463 increase of porosity of the reaction region and more motivation of upward melt flow. This
464 potentially produces positive feedback between the reaction and melt flow, contributing to
465 upward infiltration of more silicate melt into the partially molten peridotite.

466 Along with the increasing melt: peridotite ratio from ~ 1.0 to ~ 1.5 , the modeled silicate
467 melt that is reacted with the peridotite shows a decrease of SiO_2 content from ~ 47.1 wt.% to \sim
468 46.7 wt.%, which is partly less than the measured ranges in our experiments with long annealing

469 time (Figure 8a). The Al_2O_3 content of silicate melt varies from ~ 13.6 wt.% to ~ 13.1 wt.%,
470 while the MgO content of melt shows a narrow variation range of ~ 11.1 wt.% to ~ 11.4 wt.%,
471 which both roughly match our experiments (Figures 8b and 8e). The possible iron loss to Pt
472 capsule in these experiments due to the incomplete isolation of separate upper and lower graphite
473 capsules with different diameters for silicate melt from Pt capsule (J. Wang et al., 2020) is likely
474 to be the main reason for the lower FeO content (Figure 8c) measured in these experiments with
475 long annealing time (> 48 h). The model suggests that silicate melt contains ~ 7.6 - 7.9 wt.% CaO
476 at the melt-peridotite of 1.0-1.5, but this range is underestimated in contrast to our measurements
477 (Figure 8d), partly because of the slight differences in the Gibbs free energy among various
478 compositional models of pyroxenes (Yao et al., 2021) may drive large errors in the CaO content
479 of clinopyroxene in the AlphaMELTS. Although there still have some weaknesses in modeling
480 the compositional evolution of melt, the use of AlphaMELTS is encouraging here and helps to
481 examine how mineral modes and chemical compositions evolve as silicate melts are added into
482 the upper peridotite part.

483 4.3 Coarsening processes of sulfide droplets

484 In a partially molten system, the nucleation/growth rate and associated size distribution of
485 sulfide droplets are vital constraints on their dynamics (Yoshino & Watson, 2005). Along with
486 the increasing annealing time, the size of sulfide droplets shows a larger increase (from $\sim 3.2 \pm$
487 $0.1 \mu\text{m}$ to $\sim 11.1 \pm 0.4 \mu\text{m}$) (Figure 5c) compared with that of the surrounding silicate minerals
488 (from $\sim 8.1 \pm 3.4 \mu\text{m}$ to $\sim 11.0 \pm 4.9 \mu\text{m}$) (Figure 4b). The growth of silicate minerals has been
489 suggested to be mostly controlled by the melt-enhanced diffusion of material, but sulfur that is
490 the one of major elements in the sulfide has a much lower diffusivity than those of other
491 elements (Freda et al., 2005; Yao & Mungall, 2021). Given that the diffusion of S rather than Fe
492 limits the growth rate of sulfide droplets (Zhang, 2015), slow growth is expected for sulfide if its
493 growth completely occurred via element diffusion. However, the estimated growth rate of sulfide
494 droplets is larger than those of silicate minerals in our measurements, suggesting that there must
495 be other mechanisms, besides the diffusion-driven growth, contributing to the fast growth of
496 sulfide droplets.

497 On the other hand, the actual 3D size distribution of sulfide droplets in the melt source
498 shows a uniform, nearly log-normal size distribution with a skewed peak to a slightly smaller

499 size than the average one (Figure 9), which can be attributed to the possible contribution of the
500 Lifshitz-Slyozov-Wagner (LSW) coarsening and the occurrence of normal grain growth (Honour
501 et al., 2019; Yoshino & Watson, 2005). Based on the classical LSW theory (Lifshitz & Slyozov,
502 1961; Wagner, 1961), the kinetics of crystal growth can be approximately described as $r \sim t^{1/m}$,
503 where r is the grain size, with the exponent $m = 3$ for a diffusion-controlled process and $m = 2$
504 under the control of an interface reaction. At 1,250 °C and 1.5 GPa, growth rates of sulfide
505 droplets are slightly slower than that predicted ($m = 2$) by the interface-reaction-controlled
506 process via a transient regime ripening before static-state ripening (Figure 5a), implying the
507 likely combination of multiple coarsening processes here (Lautze et al., 2011; Sun, 2007). High
508 run temperature (1,300 °C) can contribute to a higher degree of interface-controlled reaction
509 (Yoshino & Watson, 2005), which potentially facilitates the coarsening processes of sulfide in
510 the melt source (Figure 5a). A dramatical decrease in the number density of sulfides (Figure 5a-
511 inset) and the presence of sulfide droplets in contact with each other (Figure 2b and Figure S1),
512 both imply that the contribution of mechanical coalescence of sulfides (agglomeration and
513 successive coalescence) to their coarsening processes may be more important at droplet contacts
514 (Yoshino & Watson, 2005). Moreover, the coalescence of sulfide droplets is enhanced at lower
515 viscous melts (Holzheid, 2010), potentially addressing a significant increase in growth rate
516 (Figure 5a) from the carbonate-bearing experiment (PC560) with a lower melt viscosity (Figure
517 8g) (Di Genova et al., 2014). Although the previous analog experiment (de Bremond d’Ars et al.,
518 2001) and static high-temperature, high-pressure experiments (Bockrath et al., 2004; Holzheid,
519 2010) did not observe the aggregation of sulfide droplets, their mechanical coalescence, for the
520 first time, has been demonstrated to be feasible in our experiments with strong melt convection
521 and melt-peridotite reaction. This mechanical coalescence may occur via the impaction of sulfide
522 droplets with each other, and further drainage and rupture of the infinitesimally liquid film
523 separating them in the reacting melt flow, as suggested by theoretical analyses (Yao et al., 2019).

524 **5 Implications**

525 5.1 Porous melt flow in the partially molten peridotite

526 These dissolution-reprecipitation processes not only change the composition and
527 proportion of solid phases, but also increase the porosity of peridotite in the upper part of
528 samples, thereby enhancing upward mobilities of silicate melt and sulfide droplets away from the

529 lower melt source (Figure 4 and Figure 5). Moreover, the porosity of ORL is enough high for the
 530 entrainment of sulfide droplets into peridotite (Figure 1 and Figure 2). In addition, with
 531 increasing annealing time to 72 h, more basaltic melt infiltrating into the peridotite region from
 532 the melt source (Figure 4) could potentially enhance the reaction between basaltic melt and
 533 peridotite. This melt-rock reaction may produce a high flow capacity of reacting melt through a
 534 dissolvable peridotite (Chadam et al., 1986; Jackson et al., 2018), resulting in the formation of
 535 the finger- or tree-like melt-rich channels in which a fast-ascending magma flow can even drive
 536 the antigravitational migration of coarse olivine grains (Pec et al., 2017). Hence, the
 537 development of positive feedback between the enhanced permeability and the associated increase
 538 of melt flux in reacting regions produces a higher flow velocity of melt and the wider melt
 539 channels among crystal framework (Aharonov, 1995; Pec et al., 2017), thereby potentially
 540 facilitating the upward entrainment of sulfide droplets (Wang & Jin, 2020).

541 To quantitatively outline the upward physical migration of sulfide droplets along with the
 542 reactive melt flows in the dissolvable peridotite, some theoretical parameters of physical
 543 properties of the partially molten peridotite should be considered first (*e.g.*, von Bagen & Waff,
 544 1986; Mckenzie, 1984). For an ideal porous crystal framework, the permeability (k) can be cast
 545 by using a power-law relationship between grain size (d) and porosity (Φ) of the crystal matrix
 546 (von Bagen & Waff, 1986):

$$547 \quad k = \frac{\Phi^n d^2}{C} \quad (2)$$

548 where C and n are constant parameters depending on the topology of the melt phase and the
 549 geometry of an individual melt channel. Based on the previous works (Miller et al., 2014; Z.
 550 Wang et al., 2020), some suitable ranges of C (36-94) and n (2.4-2.8) are used for our
 551 experiments that contain the multiphase-mineral assemblage.

552 On the basis of the numerical model from McKenzie (1989), the extraction velocity of
 553 melt relative to the stationary crystal framework can be estimated by:

$$554 \quad v = \frac{k \Delta \rho_m g}{\Phi \mu_m}$$

555 (3)

556 where $\Delta\rho_m$ - the density contrast between silicate melt and solid mineral, g - the gravitational
 557 acceleration, and μ_m - the melt viscosity, which decreases with increasing temperature and
 558 volatile content (mainly CO₂ and H₂O) (Dingwell, 1996; Di Genova et al., 2014). Based on
 559 equation (2) and (3), the porous flow velocity of melt through grain-scale percolation is ~ 0.74
 560 $\mu\text{m/h}$ in the partially molten peridotite of experiment PC545 ($C \sim 36$, $n \sim 2.6$, Miller et al., 2014;
 561 $\Phi \sim 7.13\%$; $\mu_m \sim 2.2\text{ Pa}\cdot\text{s}$; $d \sim 11.0\ \mu\text{m}$; $\Delta\rho_m \sim 600\text{ kg/m}^3$, $g \sim 9.8\text{ m/s}^2$). Apparently, the
 562 transport distance ($\sim 53.3\ \mu\text{m}$) of this slow-extracting ($\sim 0.74\ \mu\text{m/h}$) melt within the longest
 563 experimental time (72 h) is much shorter than the region of melt-peridotite reaction observed
 564 here (Figure 1a), which implies that other mechanisms of melt extraction occur concurrently to
 565 drive a higher flow velocity. In addition to the melt junctions among minerals, we also observed
 566 thick melt channels (Figure 2) between some opening mineral grain boundaries in the ORL and
 567 olivine + melt layer where a new crystal framework may have not been built, indicating the
 568 possible existence of melt channelized flow, which has been demonstrated by some experimental
 569 studies (e.g., Pec et al., 2017; Zhu et al., 2011) and the field investigations on dunite channels in
 570 MORB (e.g., Kelemen et al., 1995). Melt velocity in these channels is suggested to be much
 571 higher relative to other regions (Pec et al., 2017; Wang & Jin, 2020).

572 We then extrapolate our experimental results to the partially molten mantle. Generally,
 573 the porosity (Φ) is approximately estimated to be $\sim 1 - 15\%$ in the partially molten peridotite
 574 (e.g., Mei et al., 2002; Yoshino et al., 2010; Zhu et al., 2011), and the regions having high-degree
 575 melt-rock reaction can obtain a higher porosity (Pec et al., 2017). Hence, the Φ in our model of
 576 the molten mantle is properly set as $3 - 20\%$. The observed grain size of upper mantle peridotite
 577 is about mm-scale (Ave Lallemand et al., 1980; Karato, 1984), and thus the crystal radius in our
 578 model is set as $\sim 1.5\text{ mm}$, which is about two orders of magnitude higher than the grain size (\sim
 579 $10\ \mu\text{m}$) in the experiments here. Therefore, the permeability of upper mantle peridotite should be
 580 much better than the estimated situation of our experiments, and consequently, the extraction
 581 velocity of melt relative to stationary crystal framework in the residual mantle increases to \sim
 582 $4.78 \times 10^{-6} - 5.62 \times 10^{-5}\text{ m/s}$ ($\sim 150.81 - 1,771.06\text{ m/year}$) with the growth of Φ from 3 to 20%,
 583 if other parameters in equation (3) remain constant. On the other hand, the melt transport
 584 velocities within the mantle were estimated to have a wide range of 1 to 1,000 m/year by
 585 analyses of uranium-series (U-series) disequilibria in lavas and Icelandic deglaciation (Katz et
 586 al., 2022; Rees Jones & Rudge, 2020; Rubin et al., 2005). The channelized melt flow potentially

587 has a higher melt extraction velocity, which can even reach $\sim 10,000$ m/year (McKenzie, 2000).
588 In contrast, recent laboratory experiments further estimate some conservative velocities of the
589 porous melt flow ($\sim 2.4 - 29.7$ m/year, Z. Wang et al., 2020; $\sim 2 - 150$ m/year, Connolly et al.,
590 2009; ~ 0.5 m/year, Zhu et al., 2011). The estimated melt velocity ($\sim 150.81 - 1,771.06$ m/year)
591 here is higher than the previous experimental results ($\sim 0.5 - 150$ m/year), but falls into the
592 potential range of melt flowing velocity ($\sim 1 - 10,000$ m/year) in the natural mantle. The wide
593 range of melt flowing velocity can be attributed to the heterogeneous grain size, various mineral
594 phases, and associated heterogeneous melt flow in natural peridotite relative to these in
595 experimental conditions.

596 The microstructure of a porous crystal framework is usually simplified as a “throat and
597 chamber” model, where the interstitial chamber pores are connected by many narrow throat
598 pores. The size distribution of these throat pores will have a great effect on the permeability of
599 the crystal framework, which in turn determines the percolation of silicate melt and the migration
600 of sulfide. Previous numerical models had demonstrated that the ratio of mean throat pore radius
601 to mineral radius decreases from 0.24 to 0.09 along with the decreasing porosity of crystal
602 framework from 35.4% to 8.3% (Sweeney & Martin, 2003). Based on this modeling result, we
603 can estimate the variations in the mean throat pore radius of the partially molten peridotite with
604 constant crystal size (~ 1.5 mm) and variable porosity due to the melt-rock reaction, which can
605 help us to trace the dynamic migration of sulfide in crystal framework.

606 5.2 Upward entrainment of fine sulfide droplets by porous melt flow

607 The physical mobility of sulfide liquids along with a sulfur-saturated silicate melt within
608 the crystal framework of partially molten peridotite largely depends on the size of sulfide
609 droplets, the permeability of crystal framework, the connectivity of melt network, and the
610 processing degree of melt-rock reaction (Z. Wang et al., 2020; Yao & Mungall, 2020). Chung &
611 Mungall (2009) simplified the downward sinking of sulfide droplets in the crystal framework,
612 and proposed that this process is mostly controlled by the relative sizes of sulfide droplets and
613 surrounding crystals within partially molten peridotite. In this regard, for the upward transport of
614 a sulfide droplet, its terminal settling velocity should be also less than the upward velocity of
615 porous melt flow, although its size has been smaller than the size of the most constricted part of
616 the melt channel or pore throat in the crystal framework. The terminal settling velocity of the

617 spherical droplet will achieve when its gravity-driven buoyance force (F_B) is balanced by the
 618 vertical drag force (F_D).

619 The melt flows passing through sulfide droplets that are nearly stranded in the melt
 620 channel or port throat, as a first approximation, is regarded as the flow of an incompressible fluid
 621 around a circular cylindrical particle (*i.e.*, the sulfide droplet) confined by two parallel flat plates
 622 (*i.e.*, the melt channel) (Figure 10a) (Lee & Fung, 1969). The drag force (F_D) acting on this
 623 sulfide droplet can be expressed by a dimensionless coefficient (f_D):

$$624 \quad F_D = f_D \times 4\pi\mu_m UR$$

625 (4)

626 where R is half the distance between the two plates, *i.e.*, the radius of the melt channel, and U is
 627 the stokes flow velocity of melt around sulfide droplet. Based on the modeling results from Lee
 628 & Fung (1969), the dimensionless coefficient, f_D , can be estimated via the ratio between R and r_s
 629 which is the radius of an initial undeformed sulfide droplet before entering the melt channel
 630 (Figure 10b). For simplification, here we assume that the spherical droplet has a radius (r_s)
 631 equaling to or being slightly higher than R , and thus the corresponding values of f_D should
 632 exceed ~ 4.8 (Figure 10b) (Lee & Fung, 1969).

633 On the other hand, dense sulfide droplet always has a trend of settling to the base of the
 634 capsule due to gravity, and the corresponding buoyancy force (F_B) can be expressed as:

$$635 \quad F_B = \frac{4}{3}\pi r_s^3 g \Delta\rho_s$$

636 (5)

637 where $\Delta\rho_s = 1,700 \text{ kg/m}^3$ is the density difference between sulfide and silicate melt (Kress et al.,
 638 2008; Z. Wang et al., 2020). Hence, the velocity of melt flow that just successfully entrains
 639 sulfide droplets whose sizes are close to that of melt channel/pore throat can be calculated via:

$$640 \quad U = \frac{F_D}{4\pi\mu_m R \cdot f_D} = \frac{F_B}{4\pi\mu_m R \cdot f_D} = \frac{r_s^3 g \Delta\rho_s}{3\mu_m R \cdot f_D}$$

641 (6)

642 Because the measured maximum radius of sulfide droplets in the upper peridotite part is
 643 $\sim 9.5 \text{ }\mu\text{m}$, the maximum value of U is estimated as $\sim 170.9 \text{ }\mu\text{m/h}$ ($\sim 1.5 \text{ m/year}$), when the R/r_s
 644 equals 1. This value can represent the localized velocity of channelized melt flow in the regions

645 of melt-rock reaction and is nearly three orders of magnitude higher than the velocity of melt
 646 porous flow ($\sim 0.74 \mu\text{m/h}$) driven by compaction of crystal framework. As the melt flow velocity
 647 is changeable due to the complex morphology of interconnected melt channels and variable fluid
 648 dynamic environments in porous peridotite (McKenzie, 1989; Miller et al., 2014; Z. Wang et al.,
 649 2020; Zhu et al., 2011), our calculation ($\sim 1.5 \text{ m/year}$) here is used as an order of magnitude
 650 estimate for the velocity of melt flow around sulfide droplet through narrow pore throat in these
 651 experiments.

652 When the porous melt flow in crystal mush has a small velocity, it may not have enough
 653 kinetic energy to overcome the gravitational settling of large sulfide droplets. Hence, in this case
 654 (the region of No. ① in Figure 11), the maximum size of the upward migrating sulfide droplet is
 655 mostly controlled by the low flow velocity when the droplet size is smaller than the pore throat at
 656 the high porosity of crystal mush. For the porous melt flow with a velocity of $\sim 5.1 \times 10^{-6} \text{ m/s}$ (\sim
 657 161 m/year), due to the balance between F_B and F_D , the corresponding sulfide droplet radius is
 658 about $98.2 \mu\text{m}$, which is less than the mean radius of pore throat in crystal mush with increasing
 659 Φ from 3 to 20% (Figure 11). Here, the maximum radius (r_s) of sulfide droplets that can pass
 660 through the crystal mush will remain at $\sim 98.2 \mu\text{m}$ even though the permeability of crystal mush
 661 has been highly improved due to the increasing porosity. When the velocity of porous melt flow
 662 increases to $\sim 11.6 \times 10^{-6} \text{ m/s}$ ($\sim 366 \text{ m/year}$), the r_s is limited by the radius of the narrow pore
 663 throat at low porosity (about $\sim 9\%$), but keeps a constant value ($\sim 148.5 \mu\text{m}$) at a higher porosity
 664 (Figure 11). A further increase in the porous melt flow velocity (e.g., $\sim 2.1 \times 10^{-5} \text{ m/s}$, ~ 662
 665 m/year) will further reduce the porosity range ($> \sim 15\%$) of which the r_s is just related to the melt
 666 flow velocity (Figure 11).

667 Once the melt velocity increases to $\sim 3.2 \times 10^{-5} \text{ m/s}$ ($\sim 1,009 \text{ m/year}$), the value of r_s due
 668 to the balance between F_B and F_D will increase to $\sim 246.7 \mu\text{m}$, which is equal to the radius of
 669 pore throat at $\Phi = 20\%$ (Figure 11). Hence, if the melt velocity is beyond this value, the
 670 motivation of porous melt flow is no longer the restriction on the upward transport of fine sulfide
 671 droplets whose sizes are less than the radius of pore throat in crystal mush with the porosity
 672 range of 3-20%. Of course, this moderate flow velocity cannot provide enough power to
 673 overcome the capillary forces preventing droplet deformation as the coarse sulfide droplets
 674 attempt to pass into pore throats narrower than themselves. Therefore, in this situation (the No.
 675 ② in Figure 11), the sizes of upward transporting sulfide droplets must be strictly no larger than

676 the pore throat size in the crystal mush. Because the mean size of the pore throat is just related to
 677 the grain size and porosity of molten peridotite based on the modeling results from Sweeney &
 678 Martin (2003), the value of r_s should be equal to the estimated pore throat size that increases
 679 from 99.7 to 246.7 μm with the increasing porosity from 3 to 20%, which is irrelevant to the melt
 680 flow velocity. Thus, the No. ② situation is represented by a black line in Figure 11, although the
 681 corresponding flow velocity may vary from $\sim 3.2 \times 10^{-5}$ m/s ($\sim 1,009$ m/year) to a much higher
 682 value (e.g., ~ 0.08 m/s, as explained below). Hence, during the melt-peridotite reaction, the
 683 accompanying melt flow in the dissolved peridotite is energetic, and its flow velocity seems to be
 684 high enough to drive the upward transport of fine μm -scale sulfide droplets (Figure 10c-right
 685 side; Figure 11).

686 5.3 Potentially upward transport of coarse sulfide droplet

687 When a coarse sulfide that is sufficiently larger than the minimum constriction of the
 688 melt channel is gradually squeezed into the small “throat” part along with the ascending reactive
 689 melt flow, the sulfide droplet will invade this throat and be changed to a pear shape having a
 690 smaller radius of curvature (Figure 10c-left side). Obviously, the upward migration of this coarse
 691 sulfide droplet in the partially molten peridotite becomes complicated, and the referred dynamic
 692 process simplistically involves a competition between buoyancy, pressure gradient, viscous,
 693 capillary, and drag forces (Yao & Mungall, 2020). This squeezing process introduces the
 694 additional capillary pressure P_c , which is a measure of the pressure discontinuity existing at the
 695 interface of two immiscible phases (Chung & Mungall, 2009). The additional pressure imposed
 696 on this deformed sulfide droplet within the squeezing process equals the difference in capillary
 697 pressure between the top and bottom interfaces of the sulfide droplet and can be calculated by:

$$698 \quad \Delta P_c = 2\gamma_{ms} \times \left(\frac{1}{r_t} - \frac{1}{r_d} \right) \quad (7)$$

699

700 where $\gamma_{ms} = 0.21$ N/m is the melt-sulfide surface tension (Mungall et al., 2015), r_t is the radius of
 701 the upper spheric cap, and r_d is the radius of the lower part of the pear-shaped droplet (Figure
 702 10c). The droplet cannot be forced through the pore throat unless this excess pressure ΔP_c is
 703 balanced by an equal or greater pressure (ΔP) exerted by ascending melt flow on the trailing
 704 edge of sulfide droplet, which tends to push the droplet to rise through the melt channel.

705 Because the silicate melt flows at a low Mach number, the simple form of Bernoulli's
 706 principle is valid for the quasi-incompressible flows in melt-peridotite reaction, and hence
 707 pressure of flowing melt around a sulfide droplet can be highly related to the peripheral flow
 708 velocity via the Bernoulli's equation (Bauman & Schwaneberg, 1994):

$$709 \quad P_1 + \frac{\rho_m U_1^2}{2} + \rho_m g h_1 = P_2 + \frac{\rho_m U_2^2}{2} + \rho_m g h_2$$

710 (8)

711 where the subscripts 1 and 2 correspond to the top and bottom outside points of deformed sulfide
 712 droplets along the axis of symmetry, respectively; P is the pressure caused by the flow of silicate
 713 melt; ρ_m is the density of melt; h is the height of 1 and 2 relative to a reference point beneath
 714 sulfide droplet. Hence, the flowing-melt-driven external pressure imposed on the deformed
 715 sulfide droplet equals the difference (ΔP) between P_1 and P_2 . In an extreme case, the coarse,
 716 deformed sulfide droplet completely blocks the ascending melt flow, and the flow velocity at
 717 bottom of droplets (U_2) is close enough to zero, leading to a maximum value of external pressure
 718 difference (ΔP) that can be calculated as:

$$719 \quad \Delta P = P_2 - P_1 = \frac{\rho_m U_1^2}{2} + \rho_m g (h_1 - h_2) = \frac{\rho_m U_1^2}{2} + \rho_m g \Delta h$$

720 (9)

721 where U_1 is the flow velocity of melt at the top of the sulfide droplet, and Δh is the vertical
 722 distance between the top and bottom points of the droplet. Assuming that the volume of a sulfide
 723 droplet is unchanged during the squeezing process, the height of this invading sulfide droplet
 724 (Δh) can be described by Chung & Mungall (2009):

$$725 \quad \Delta h = r_t + r_d + \sqrt{r_d^2 - R^2} - \sqrt{r_t^2 - R^2}$$

726 (10)

727 For the deformed sulfide droplet, it bears the upward pressure driven by flow melt (*i.e.*,
 728 ΔP), which should balance or even exceed the total of downward capillary pressure (ΔP_C) and
 729 gravity-driven pressure (P_G) for the droplet to rise through the constriction:

$$730 \quad \Delta P \geq P_G + \Delta P_C = \rho_s g \Delta h + 2\gamma_{ms} \times \left(\frac{1}{r_t} - \frac{1}{r_d} \right)$$

731 (11)

732 where ρ_s is the density of sulfide liquid. Thus, combining the above equations (7-10), under the
 733 critical condition for migration of sulfide droplet into the pore throat to be the case ($r_t = R$)
 734 (Chung & Mungall, 2009), the equation 11 substituted with the appropriate values for $\rho_m = 2,600$
 735 kg/m^3 (Robertson et al., 2016) is simplified into:

$$736 \quad 1,300 \times U_1^2 \geq 16,660 \times \left(R + r_d + \sqrt{r_d^2 - R^2} \right) + 0.42 \times \left(\frac{1}{R} - \frac{1}{r_d} \right)$$

737 (12)

738 And finally, the initial radius (r_s) of this sulfide droplet before its invasion into the pore throat
 739 can be calculated by Chung & Mungall (2009):

$$740 \quad r_s = \left(0.5 \times (r_d^3 + R^3 + (r_d^2 + \frac{1}{2}R^2) \times \sqrt{r_d^2 - R^2}) \right)^{1/3}$$

741 (13)

742 When the melt flows around a sulfide droplet through a narrow pore throat in the partially
 743 molten peridotite, the associated velocity field is suggested to be not homogeneous. In addition,
 744 it is well known that exactly deciphering the flow velocity field of silicate melt infiltrating
 745 through a multi-mineral phase system plays a critically important role in understanding the
 746 geodynamic properties of the partially molten upper mantle, but it is challenging and beyond the
 747 scope of this study. The increases in grain size and permeability may also strongly enhance the
 748 melt flow velocity in the new channel of the crystal framework. Here, the flow velocity in the
 749 channel has been confirmed to be about three orders of magnitude higher than that of porous
 750 flow through grain-scale percolation in our experiments, which may be extrapolated to the mm-
 751 scale upper mantle peridotite. Therefore, the velocity of melt flow around a sulfide droplet in the
 752 channel in upper mantle peridotite may be in the magnitude of 0.001-0.1 m/s, and thus the local
 753 velocity (U_l) of focused melt flow around the top of a sulfide droplet was analogously assumed
 754 as ~ 0.3 m/s and ~ 0.08 m/s here (Figure 11- region ③) for the localized high-degree melt-rock
 755 reaction regions of the partially molten mantle. This range of flow velocity is also consistent with
 756 the estimates from previous studies discussed in Section 5.1.

757 Equations 12 and 13 are numerically solved for the above value of U_l by programming a
 758 loop using Maple[®]. Based on the above numerical calculation, when the velocity of focused melt
 759 flow around a sulfide droplet is less than ~ 0.08 m/s, the sulfide droplet is difficult to overcome
 760 the capillary pressure imposed by melt channel/pore throat with a smaller size, and will be

761 stranded in inter-grain pores. However, these flow velocities ($\sim 3.2 \times 10^{-5}$ m/s – 0.08 m/s) are
762 still large enough to drive upward transport of sulfide droplets whose radii are smaller than or
763 almost the same as the radius (R) of pore throat (Figure 11-region ②).

764 For a powerful melt flow with extremely high velocity (e.g., ~ 0.3 m/s in Figure 11-
765 region ③), coarse-grained sulfide droplet overcomes the capillary pressure driven by the pore
766 throat, and its maximum radius for upward migration increases from ~ 106.8 to ~ 276.8 μm with
767 increasing the porosity from 3 % to 20 % (Figure 11-region ③), which is larger than the
768 corresponding radius of the pore throat (from ~ 99.7 to 246.7 μm). In this condition (region ③ in
769 Figure 11), the coarse sulfide droplets can pass through the pore throat narrower than themselves.
770 Although the estimates of the maximum sulfide size that are capable of upward migrating
771 through the porous molten peridotite are divided into three conditions along with the increasing
772 melt flow velocity (the regions ①-③ in Figure 11), all of them are mostly dominated by the melt
773 flow velocity, porosity, and grain size of peridotite, which would be strongly enhanced by the
774 high-degree melt-rock reaction.

775 On the other hand, based on these previous studies on the abyssal and orogenic
776 peridotites, and peridotite xenoliths (e.g., Lorand & Luguet, 2016; Lorand et al., 2010; Luguet et
777 al., 2003), highly variable grain size (< 20 μm to 500 μm) of sulfides is widely observed in the
778 upper mantle, while most sulfides are likely smaller than about 100 μm in diameter. Hence, it is
779 plausible that almost all sulfide droplets are stranded among the crystal framework of the upper
780 peridotite mantle with low porosity, while the high-degree partial melting and/or melt-peridotite
781 reaction will lead to high porosity, large flow velocity, and even the new-forming melt channel,
782 which highly proposes that efficient entrainment of most sulfide droplets into ascending magma
783 flow among porous peridotite is physically possible, especially among channelized extraction of
784 silicate melt in melt-peridotite reaction. Conceivably, mechanical entrainment of sulfide droplets
785 during the melt-rock reaction would be more efficient than the transport of sulfide liquid by
786 dissolving in departing silicate melt, especially given the slow S diffusion in the basaltic melt
787 (Freda et al., 2005). The sub-continental lithospheric mantle that undergoes large-scale partial
788 melting and melt-peridotite reaction under tectonically active craton margins may be favorable
789 conjunction of these factors and potentially conducive to the entrainment of large sulfide droplets,
790 thereby contributing to the fertilization of sub-continental lithospheric mantle and the primary
791 enrichment of metal-bearing sulfides for the formation of magmatic sulfide deposits (e.g., Griffin

792 et al., 2013). This may be one of the reasons to account for the issue of why the spatial and
793 temporal distribution of magmatic Ni-Cu-(PGE) sulfide deposits are genetically related to these
794 regions (Maier & Groves, 2011).

795 **6 Conclusions**

796 Reaction-infiltration of silicate melt and concomitant transport of sulfide droplets in the
797 partially molten peridotite are examined experimentally and thermodynamical-quantitatively in
798 this study, which provides important insights into the fertilization of sub-continental lithospheric
799 mantle and the efficient recycling of sulfur and metal elements from the partially molten mantle.
800 The reaction between peridotite and basalt leads to the preferential dissolution of olivine and
801 precipitation of orthopyroxene at high temperature (1,250-1,300 °C) and pressure (1.5 GPa),
802 forming an orthopyroxene-rich reaction layer (ORL) with a high growth rate ($\sim 0.78 \pm 0.05$
803 $\mu\text{m/s}^{0.5}$ at 1,250 °C) in the melt-rock interface. With increasing the degree of melt-peridotite
804 reaction, more silicate melt infiltrates through the ORL into the upper partially molten peridotite,
805 forming an olivine-melt layer above the ORL, and coarse sulfide droplets could also be entrained
806 along with the infiltration of silicate melt. Systematic variations observed in the compositions of
807 minerals and reactive melt are approximately consistent with the thermodynamically-constrained
808 mixing model. Meanwhile, the sizes of sulfide droplets have fast growth in the melt source,
809 which is partly attributed to the multiple coarsening processes (including the mechanical
810 coalescence) of sulfide droplets in the dynamic reactive melt flow.

811 Suspension and entrainment of sulfide droplets in the partially molten peridotite indicate
812 a fast-flowing velocity of reactive melt ($\sim 170.9 \mu\text{m/h}$) in our experiments, which demonstrates
813 the occurrence of focused melt flows with high velocity in the reactive-forming melt channels,
814 besides the melt porous flow driven by the density difference between silicate melt and minerals
815 forming the crystal framework. It is convincible that the melt flow velocity within the melt-rock
816 reaction is potentially high enough to drive upward transport of fine sulfide droplets with smaller
817 diameters than that of the pore throat in the partially molten peridotite. In this condition, the
818 maximum size of sulfide for upward entrainment is limited by the radius of the pore throat in the
819 crystal framework of peridotite and increases with the growth of porosity during partial melting
820 and melt-peridotite reaction. Only in the channelized melt flow with extremely high velocity,
821 coarse-grained sulfide droplets could upward migrate through the pore throats narrower than

822 themselves. Hence, the high-degree melt-rock reaction regions in the upper mantle, such as the
823 sub-continental lithospheric mantle of craton margins, are likely to have wide pore throats, high
824 porosity, and even channelized melt flow with high velocity, which can potentially drive upward
825 entrainment and/or extrusion of sulfide droplets in the partially molten mantle, and thereby
826 fertilize the lithospheric mantle and lead to the endowment of Cu- and Ni-bearing sulfide for the
827 formation of associated deposits.

828 **Acknowledgments**

829 We are grateful to two anonymous reviewers for their useful suggestions and comments. We
830 thank Prof. Zhang Jinsen and Dr. Wenlong Liu for their help with EPMA and EBSD analysis.
831 Especially, I appreciate my wife Shasha Guo for the support and help in my life, so that I could
832 do my research without any worries. This research was supported by the National Natural
833 Science Foundation of China (No. 42102057, 42272084, and 41902088), the Natural Science
834 Foundation of Hebei Province (No. D2021402019), the fund from SinoProbe Laboratory (No.
835 SinoProbe Lab 202219), and the Education Department Foundation of Hebei Province of China
836 (BJ2020023).

837 **Data Availability Statement**

838 Microprobe images used for the composition measurements and all data are shown in figures and
839 the supplemental materials are freely available online
840 (<https://doi.org/10.6084/m9.figshare.22352632>).

841 **References**

- 842 Aharonov, E. (1995). Channeling instability of upwelling melt in the mantle. *Journal of*
843 *Geophysical Research: Solid Earth*, 100(B10), 20433–20450.
844 <https://doi.org/10.1029/95JB01307>
- 845 Alard, O., Lorand, J. P., Reisberg, L., Bodinier, J. L., Dautria, J. M., & O'Reilly, S. Y. (2011).
846 Volatile-rich metasomatism in Montferrier xenoliths (Southern France): Implications for the
847 abundances of chalcophile and highly siderophile elements in the subcontinental mantle.
848 *Journal of Petrology*, 52(10), 2009–2045. <https://doi.org/10.1093/petrology/egr038>

- 849 Ave Lallemand, H. G., Mercier, J.-C. C., Carter, N. L., & Ross, J. V. (1980). Rheology of the
850 upper mantle: Inferences from peridotite xenoliths. *Tectonophysics*, 70(1–2), 85–113.
851 [https://doi.org/10.1016/0040-1951\(80\)90022-0](https://doi.org/10.1016/0040-1951(80)90022-0)
- 852 Bagdassarov, N., Solferino, G., Golabek, G. J., & Schmidt, M. W. (2009). Centrifuge assisted
853 percolation of Fe–S melts in partially molten peridotite: Time constraints for planetary core
854 formation. *Earth and Planetary Science Letters*, 288(1–2), 84–95.
855 <https://doi.org/10.1016/j.epsl.2009.09.010>
- 856 Ballhaus, C., Bockrath, C., Wohlgemuth-Ueberwasser, C., Laurenz, V., & Berndt, J. (2006).
857 Fractionation of the noble metals by physical processes. *Contributions to Mineralogy and
858 Petrology*, 152(6), 667–684. <https://doi.org/10.1007/s00410-006-0126-z>
- 859 Bauman, R. P., & Schwaneberg, R. (1994). Interpretation of Bernoulli’s equation. *The Physics
860 Teacher*, 32(8), 478–488. <https://doi.org/10.1119/1.2344087>
- 861 Bockrath, C., Ballhaus, C., & Holzheid, A. (2004). Fractionation of the platinum-group elements
862 during mantle melting. *Science*, 305(5692), 1951–1953.
863 <https://doi.org/10.1126/science.1100160>
- 864 Cascio, M. Lo, Liang, Y., Shimizu, N., & Hess, P. C. (2008). An experimental study of the grain-
865 scale processes of peridotite melting: Implications for major and trace element distribution
866 during equilibrium and disequilibrium melting. *Contributions to Mineralogy and Petrology*,
867 156(1), 87–102. <https://doi.org/10.1007/s00410-007-0275-8>
- 868 Chadam, J., Hoff, D., Merino, E., Ortoleva, P., & Sen, A. (1986). Reactive infiltration
869 instabilities. *IMA Journal of Applied Mathematics (Institute of Mathematics and Its
870 Applications)*, 36(3), 207–221. <https://doi.org/10.1093/imamat/36.3.207>
- 871 Chen, C., Yao, Z. S., Wang, C. Y. (2022). Partitioning behaviors of cobalt and manganese along
872 diverse melting paths of peridotitic and MORB-like pyroxenitic mantle. *Journal of Petrology*,
873 63, 1–22. <https://doi.org/10.1093/petrology/egac021>
- 874 Chowdhury, P., & Dasgupta, R. (2020). Sulfur extraction via carbonated melts from sulfide-
875 bearing mantle lithologies – Implications for deep sulfur cycle and mantle redox. *Geochimica
876 et Cosmochimica Acta*, 269, 376–397. <https://doi.org/10.1016/j.gca.2019.11.002>
- 877 Chung, H. Y., & Mungall, J. E. (2009). Physical constraints on the migration of immiscible
878 fluids through partially molten silicates, with special reference to magmatic sulfide ores. *Earth
879 and Planetary Science Letters*, 286(1–2), 14–22. <https://doi.org/10.1016/j.epsl.2009.05.041>

- 880 Ciazela, J., Koepke, J., Dick, H. J. B., Botcharnikov, R., Muszynski, A., Lazarov, M., et al.
881 (2018). Sulfide enrichment at an oceanic crust-mantle transition zone: Kane Megamullion
882 (23°N, MAR). *Geochimica et Cosmochimica Acta*, 230, 155–189.
883 <https://doi.org/10.1016/j.gca.2018.03.027>
- 884 Connolly, J. A. D., Schmidt, M. W., Solferino, G., & Bagdassarov, N. (2009). Permeability of
885 asthenospheric mantle and melt extraction rates at mid-ocean ridges. *Nature*, 462(7270), 209–
886 212. <https://doi.org/10.1038/nature08517>
- 887 Daines, M. J., & Kohlstedt, D. L. (1994). The transition from porous to channelized flow due to
888 melt/rock reaction during melt migration. *Geophysical Research Letters*, 21(2), 145–148.
889 <https://doi.org/10.1029/93GL03052>
- 890 de Bremond d’Ars, J., Arndt, N. T., & Hallot, E. (2001). Analog experimental insights into the
891 formation of magmatic sulfide deposits. *Earth and Planetary Science Letters*, 186(3–4), 371–
892 381. [https://doi.org/10.1016/S0012-821X\(01\)00254-0](https://doi.org/10.1016/S0012-821X(01)00254-0)
- 893 Di Genova, D., Romano, C., Alletti, M., Misiti, V., & Scarlato, P. (2014). The effect of CO₂ and
894 H₂O on Etna and Fondo Riccio (Phlegrean Fields) liquid viscosity, glass transition
895 temperature and heat capacity. *Chemical Geology*, 377, 72–86.
896 <https://doi.org/10.1016/j.chemgeo.2014.04.001>
- 897 Ding, S., & Dasgupta, R. (2017). The fate of sulfide during decompression melting of peridotite
898 – implications for sulfur inventory of the MORB-source depleted upper mantle. *Earth and*
899 *Planetary Science Letters*, 459, 183–195. <https://doi.org/10.1016/j.epsl.2016.11.020>
- 900 Dingwell, D. B. (1996). Volcanic Dilemma--Flow or Blow? *Science*, 273(5278), 1054–1055.
901 <https://doi.org/10.1126/science.273.5278.1054>
- 902 Farquhar, J., Wing, B. A., McKeegan, K. D., Harris, J. W., Cartigny, P., & Thiemens, M. H.
903 (2002). Mass-independent sulfur of inclusions in diamond and sulfur recycling on early Earth.
904 *Science*, 298(5602), 2369–2372. <https://doi.org/10.1126/science.1078617>
- 905 Faul, U. H. (2001). Melt retention and segregation beneath mid-ocean ridges. *Nature*, 410(6831),
906 920–923. <https://doi.org/10.1038/35073556>
- 907 Faul, U. H., & Scott, D. (2006). Grain growth in partially molten olivine aggregates.
908 *Contributions to Mineralogy and Petrology*, 151(1), 101–111. [https://doi.org/10.1007/s00410-](https://doi.org/10.1007/s00410-005-0048-1)
909 005-0048-1

- 910 Freda, C., Baker, D. R., & Scarlato, P. (2005). Sulfur diffusion in basaltic melts. *Geochimica et*
911 *Cosmochimica Acta*, 69(21), 5061–5069. <https://doi.org/10.1016/j.gca.2005.02.002>
- 912 Ghiorso, M. S., & Sack, R. O. (1995). Chemical mass transfer in magmatic processes IV. A
913 revised and internally consistent thermodynamic model for the interpolation and extrapolation
914 of liquid-solid equilibria in magmatic systems at elevated temperatures and pressures.
915 *Contributions to Mineralogy and Petrology*, 119(2–3), 197–212.
916 <https://doi.org/10.1007/BF00307281>
- 917 Ghiorso, M. S., Hirschmann, M. M., Reiners, P. W., & Kress, V. C. (2002). The pMELTS: A
918 revision of MELTS for improved calculation of phase relations and major element partitioning
919 related to partial melting of the mantle to 3 GPa. *Geochemistry, Geophysics, Geosystems*, 3(5),
920 1–35. <https://doi.org/10.1029/2001gc000217>
- 921 Giordano, D., Russell, J. K., & Dingwell, D. B. (2008). Viscosity of magmatic liquids: A model.
922 *Earth and Planetary Science Letters*, 271(1–4), 123–134.
923 <https://doi.org/10.1016/j.epsl.2008.03.038>
- 924 Griffin, W. L., Begg, G. C., & O'Reilly, S. Y. (2013). Continental-root control on the genesis of
925 magmatic ore deposits. *Nature Geoscience*, 6(11), 905–910. <https://doi.org/10.1038/ngeo1954>
- 926 Heinrich, C. A., & Connolly, J. A. D. (2022). Physical transport of magmatic sulfides promotes
927 copper enrichment in hydrothermal ore fluids. *Geology*, 50(10), 1101–1105.
928 <https://doi.org/10.1130/G50138.1>
- 929 Higgins, M. D. (1998). Origin of Anorthosite by Textural Coarsening: Quantitative
930 Measurements of a Natural Sequence of Textural Development. *Journal of Petrology*, 39(7),
931 1307–1323. <https://doi.org/10.1093/petrology/39.7.1307>
- 932 Higgins, M. D. (2011). Textural coarsening in igneous rocks. *International Geology Review*,
933 53(3–4), 354–376. <https://doi.org/10.1080/00206814.2010.496177>
- 934 Holwell, D. A., Fiorentini, M. L., Knott, T. R., McDonald, I., Blanks, D. E., Campbell McCuaig,
935 T., & Gorczyk, W. (2022). Mobilisation of deep crustal sulfide melts as a first order control on
936 upper lithospheric metallogeny. *Nature Communications*, 13(1).
937 <https://doi.org/10.1038/s41467-022-28275-y>
- 938 Holzheid, A. (2010). Separation of sulfide melt droplets in sulfur saturated silicate liquids.
939 *Chemical Geology*, 274(3–4), 127–135. <https://doi.org/10.1016/j.chemgeo.2010.03.005>

- 940 Holzheid, A., & Grove, T. L. (2002). Sulfur saturation limits in silicate melts and their
941 implications for core formation scenarios for terrestrial planets. *American Mineralogist*, 87(2–
942 3), 227–237. <https://doi.org/10.2138/am-2002-2-304>
- 943 Holzheid, A., Schmitz, M. D., & Grove, T. L. (2000). Textural equilibria of iron sulfide liquids
944 in partly molten silicate aggregates and their relevance to core formation scenarios. *Journal of*
945 *Geophysical Research: Solid Earth*, 105(B6), 13555–13567.
946 <https://doi.org/10.1029/2000JB900046>
- 947 Honour, V. C., Holness, M. B., Partridge, J. L., & Charlier, B. (2019). Microstructural evolution
948 of silicate immiscible liquids in ferrobasalts. *Contributions to Mineralogy and Petrology*,
949 174(9). <https://doi.org/10.1007/s00410-019-1610-6>
- 950 Iacono-Marziano, G., Le Vaillant, M., Godel, B. M., Barnes, S. J., & Arbaret, L. (2022). The
951 critical role of magma degassing in sulphide melt mobility and metal enrichment. *Nature*
952 *Communications*, 13(1). <https://doi.org/10.1038/s41467-022-30107-y>
- 953 Jackson, M. D., Blundy, J., & Sparks, R. S. J. (2018). Chemical differentiation, cold storage and
954 remobilization of magma in the Earth’s crust. *Nature*, 564(7736), 405–409.
955 <https://doi.org/10.1038/s41586-018-0746-2>
- 956 Karato, S.-I. (1984). Grain-size distribution and rheology of the upper mantle. *Tectonophysics*,
957 104(1–2), 155–176. [https://doi.org/10.1016/0040-1951\(84\)90108-2](https://doi.org/10.1016/0040-1951(84)90108-2)
- 958 Katz, R. F., Jones, D. W. R., Rudge, J. F., & Keller, T. (2022). Physics of Melt Extraction from
959 the Mantle: Speed and Style. *Annual Review of Earth and Planetary Sciences*, 50, 507–540.
960 <https://doi.org/10.1146/annurev-earth-032320-083704>
- 961 Kelemen, P. B., Shimizu, N., & Salters, V. J. M. (1995). Extraction of mid-ocean-ridge basalt
962 from the upwelling mantle by focused flow of melt in dunite channels. *Nature*, 375(6534),
963 747–753. <https://doi.org/10.1038/375747a0>
- 964 Kress, V., Greene, L. E., Ortiz, M. D., & Mioduszewski, L. (2008). Thermochemistry of sulfide
965 liquids IV: Density measurements and the thermodynamics of O-S-Fe-Ni-Cu liquids at low to
966 moderate pressures. *Contributions to Mineralogy and Petrology*, 156(6), 785–797.
967 <https://doi.org/10.1007/s00410-008-0315-z>
- 968 Lambart, S., Laporte, D., Provost, A., & Schiano, P. (2012). Fate of pyroxenite-derived melts in
969 the peridotitic mantle: Thermodynamic and experimental constraints. *Journal of Petrology*,
970 53(3), 451–476. <https://doi.org/10.1093/petrology/egr068>

- 971 Lautze, N. C., Sisson, T. W., Mangan, M. T., & Grove, T. L. (2011). Segregating gas from melt:
972 An experimental study of the Ostwald ripening of vapor bubbles in magmas. *Contributions to*
973 *Mineralogy and Petrology*, 161(2), 331–347. <https://doi.org/10.1007/s00410-010-0535-x>
- 974 Lee, C. T. A., & Tang, M. (2020). How to make porphyry copper deposits. *Earth and Planetary*
975 *Science Letters*, 529, 115868. <https://doi.org/10.1016/j.epsl.2019.115868>
- 976 Lee, J. S., & Fung, Y. C. (1969). Stokes flow around a circular cylindrical post confined between
977 two parallel plates. *Journal of Fluid Mechanics*, 37(4), 657–670.
978 <https://doi.org/10.1017/S0022112069000796>
- 979 Liang, Y. (1999). Diffusive dissolution in ternary systems: Analysis with applications to quartz
980 and quartzite dissolution in molten silicates. *Geochimica et Cosmochimica Acta*, 63(23–24),
981 3983–3995. [https://doi.org/10.1016/s0016-7037\(99\)00203-3](https://doi.org/10.1016/s0016-7037(99)00203-3)
- 982 Lifshitz, I. M., & Slyozov, V. V. (1961). The kinetics of precipitation from supersaturated solid
983 solutions. *Journal of Physics and Chemistry of Solids*, 19(1–2), 35–50.
984 [https://doi.org/10.1016/0022-3697\(61\)90054-3](https://doi.org/10.1016/0022-3697(61)90054-3)
- 985 Liu, Y., Samaha, N.-T., & Baker, D. R. (2007). Sulfur concentration at sulfide saturation (SCSS)
986 in magmatic silicate melts. *Geochimica et Cosmochimica Acta*, 71(7), 1783–1799.
987 <https://doi.org/10.1016/j.gca.2007.01.004>
- 988 Lorand, J. P., & Luguet, A. (2016). Chalcophile and siderophile elements in Mantle Rocks:
989 Trace elements controlled by trace minerals. *Reviews in Mineralogy and Geochemistry*, 81(1),
990 441–488. <https://doi.org/10.2138/rmg.2016.81.08>
- 991 Lorand, J. P., Alard, O., & Luguet, A. (2010). Platinum-group element micronuggets and
992 refertilization process in Lherz orogenic peridotite (northeastern Pyrenees, France). *Earth and*
993 *Planetary Science Letters*, 289(1–2), 298–310. <https://doi.org/10.1016/j.epsl.2009.11.017>
- 994 Luguet, A., Lorand, J. P., & Seyler, M. (2003). Sulfide petrology and highly siderophile element
995 geochemistry of abyssal peridotites: A coupled study of samples from the Kane Fracture Zone
996 (45°W 23°20N, MARK area, Atlantic Ocean). *Geochimica et Cosmochimica Acta*, 67(8),
997 1553–1570. [https://doi.org/10.1016/S0016-7037\(02\)01133-X](https://doi.org/10.1016/S0016-7037(02)01133-X)
- 998 Mallik, A., & Dasgupta, R. (2012). Reaction between MORB-eclogite derived melts and fertile
999 peridotite and generation of ocean island basalts. *Earth and Planetary Science Letters*, 329–
1000 330, 97–108. <https://doi.org/10.1016/j.epsl.2012.02.007>

- 1001 Mavrogenes, J. A., & O'Neill, H. S. C. (1999). The relative effects of pressure, temperature and
1002 oxygen fugacity on the solubility of sulfide in mafic magmas. *Geochimica et Cosmochimica*
1003 *Acta*, 63(7–8), 1173–1180. [https://doi.org/10.1016/S0016-7037\(98\)00289-0](https://doi.org/10.1016/S0016-7037(98)00289-0)
- 1004 Mckenzie, D. (1984). The generation and compaction of partially molten rock. *Journal of*
1005 *Petrology*, 25(3), 713–765. <https://doi.org/10.1093/petrology/25.3.713>
- 1006 McKenzie, D. (1989). Some remarks on the movement of small melt fractions in the mantle.
1007 *Earth and Planetary Science Letters*, 95(1–2), 53–72. [https://doi.org/10.1016/0012-](https://doi.org/10.1016/0012-821X(89)90167-2)
1008 [821X\(89\)90167-2](https://doi.org/10.1016/0012-821X(89)90167-2)
- 1009 McKenzie, D. (2000). Constraints on melt generation and transport from U-series activity ratios.
1010 *Chemical Geology*, 162(2), 81–94. [https://doi.org/10.1016/S0009-2541\(99\)00126-6](https://doi.org/10.1016/S0009-2541(99)00126-6)
- 1011 Médard, E., McCammon, C. A., Barr, J. A., & Grove, T. L. (2008). Oxygen fugacity,
1012 temperature reproducibility, and H₂O contents of nominally anhydrous piston-cylinder
1013 experiments using graphite capsules. *American Mineralogist*, 93(11–12), 1838–1844.
1014 <https://doi.org/10.2138/am.2008.2842>
- 1015 Mei, S., Bai, W., Hiraga, T., & Kohlstedt, D. L. (2002). Influence of melt on the creep behavior
1016 of olivine-basalt aggregates under hydrous conditions. *Earth and Planetary Science Letters*,
1017 201(3–4), 491–507. [https://doi.org/10.1016/S0012-821X\(02\)00745-8](https://doi.org/10.1016/S0012-821X(02)00745-8)
- 1018 Mercier, M., Muro, A. di, Métrich, N., Giordano, D., Belhadj, O., & Mandeville, C. W. (2010).
1019 Spectroscopic analysis (FTIR, Raman) of water in mafic and intermediate glasses and glass
1020 inclusions. *Geochimica et Cosmochimica Acta*, 74(19), 5641–5656.
1021 <https://doi.org/10.1016/j.gca.2010.06.020>
- 1022 Milke, R., Abart, R., Kunze, K., Koch-Müller, M., Schmid, D., & Ulmer, P. (2009). Matrix
1023 rheology effects on reaction rim growth I: Evidence from orthopyroxene rim growth
1024 experiments. *Journal of Metamorphic Geology*, 27(1), 71–82. [https://doi.org/10.1111/j.1525-](https://doi.org/10.1111/j.1525-1314.2008.00804.x)
1025 [1314.2008.00804.x](https://doi.org/10.1111/j.1525-1314.2008.00804.x)
- 1026 Miller, K. J., Zhu, W., Montési, L. G. J., & Gaetani, G. A. (2014). Experimental quantification of
1027 permeability of partially molten mantle rock. *Earth and Planetary Science Letters*, 388, 273–
1028 282. <https://doi.org/10.1016/j.epsl.2013.12.003>
- 1029 Mitchell, A. L., & Grove, T. L. (2016). Experiments on melt–rock reaction in the shallow mantle
1030 wedge. *Contributions to Mineralogy and Petrology*, 171(12). [https://doi.org/10.1007/s00410-](https://doi.org/10.1007/s00410-016-1312-2)
1031 [016-1312-2](https://doi.org/10.1007/s00410-016-1312-2)

- 1032 Morgan, Z., & Liang, Y. (2003). An experimental and numerical study of the kinetics of
1033 harzburgite reactive dissolution with applications to dunite dike formation. *Earth and*
1034 *Planetary Science Letters*, 214(1–2), 59–74. [https://doi.org/10.1016/S0012-821X\(03\)00375-3](https://doi.org/10.1016/S0012-821X(03)00375-3)
- 1035 Morgan, Z., & Liang, Y. (2005). An experimental study of the kinetics of lherzolite reactive
1036 dissolution with applications to melt channel formation. *Contributions to Mineralogy and*
1037 *Petrology*, 150(4), 369–385. <https://doi.org/10.1007/s00410-005-0033-8>
- 1038 Mungall, J. E., Brenan, J. M., Godel, B., Barnes, S. J., & Gaillard, F. (2015). Transport of metals
1039 and sulphur in magmas by flotation of sulphide melt on vapour bubbles. *Nature Geoscience*,
1040 8(3), 216–219. <https://doi.org/10.1038/ngeo2373>
- 1041 Mungall, J. E. (2002). Empirical models relating viscosity and tracer diffusion in magmatic
1042 silicate melts. *Geochimica et Cosmochimica Acta*, 66(1), 125–143.
1043 [https://doi.org/10.1016/S0016-7037\(01\)00736-0](https://doi.org/10.1016/S0016-7037(01)00736-0)
- 1044 Mungall, J. E., & Brenan, J. M. (2014). Partitioning of platinum-group elements and Au between
1045 sulfide liquid and basalt and the origins of mantle-crust fractionation of the chalcophile
1046 elements. *Geochimica et Cosmochimica Acta*, 125, 265–289.
1047 <https://doi.org/10.1016/j.gca.2013.10.002>
- 1048 Niu, Y. (2004). Bulk-rock major and trace element compositions of abyssal peridotites:
1049 Implications for mantle melting, melt extraction and post-melting processes beneath Mid-
1050 Ocean ridges. *Journal of Petrology*, 45(12), 2423–2458.
1051 <https://doi.org/10.1093/petrology/egh068>
- 1052 Pan, F., Zhang, H., He, X., Harris, N., Dai, H.K., Xiong, Q., Luo, B., Liu, D., Kusky, T., &
1053 Sadiq, I. (2023). Lithosphere tearing and foundering during continental subduction: insights
1054 from Oligocene-Miocene magmatism in southern Tibet. *GSA Bulletin*,
1055 <https://doi.org/10.1130/B36746.1>
- 1056 Patten, C., Barnes, S. J., Mathez, E. A., & Jenner, F. E. (2013). Partition coefficients of
1057 chalcophile elements between sulfide and silicate melts and the early crystallization history of
1058 sulfide liquid: LA-ICP-MS analysis of MORB sulfide droplets. *Chemical Geology*, 358, 170–
1059 188. <https://doi.org/10.1016/j.chemgeo.2013.08.040>
- 1060 Pec, M., Holtzman, B. K., Zimmerman, M. E., & Kohlstedt, D. L. (2015). Reaction infiltration
1061 instabilities in experiments on partially molten mantle rocks. *Geology*, 43(7), 575–578.
1062 <https://doi.org/10.1130/G36611.1>

- 1063 Pec, M., Holtzman, B. K., Zimmerman, M. E., & Kohlstedt, D. L. (2017). Reaction infiltration
1064 instabilities in mantle rocks: An experimental investigation. *Journal of Petrology*, *58*(5), 979–
1065 1003. <https://doi.org/10.1093/petrology/egx043>
- 1066 Pin, J., France, L., Lambart, S., & Reisberg, L. (2022). Thermodynamic modeling of melt
1067 addition to peridotite: Implications for the refertilization of the non-cratonic continental
1068 mantle lithosphere. *Chemical Geology*, *609*, 121050.
1069 <https://doi.org/10.1016/j.chemgeo.2022.121050>
- 1070 Rees Jones, D. W., & Rudge, J. F. (2020). Fast magma ascent, revised estimates from the
1071 deglaciation of Iceland. *Earth and Planetary Science Letters*, *542*, 116324.
1072 <https://doi.org/10.1016/j.epsl.2020.116324>
- 1073 Robertson, J. C., Barnes, S. J., & Le Vaillant, M. (2016). Dynamics of magmatic sulphide
1074 droplets during transport in silicate melts and implications for magmatic sulphide ore
1075 formation. *Journal of Petrology*, *56*(12), 2445–2472. <https://doi.org/10.1093/petrology/egv078>
- 1076 Rubin, K. H., van der Zander, I., Smith, M. C., & Bergmanis, E. C. (2005). Minimum speed limit
1077 for ocean ridge magmatism from ^{210}Pb – ^{226}Ra – ^{230}Th disequilibria. *Nature*, *437*(7058), 534–
1078 538. <https://doi.org/10.1038/nature03993>
- 1079 Shaw, C. S. J., Lebert, B. S., & Woodland, A. B. (2018). Thermodynamic modelling of mantle-
1080 melt interaction evidenced by veined wehrlite xenoliths from the Rockeskyllerkopf Volcanic
1081 Complex, West Eifel volcanic field, Germany. *Journal of Petrology*, *59*(1), 59–86.
1082 <https://doi.org/10.1093/petrology/egy018>
- 1083 Smith, P. M., & Asimow, P. D. (2005). Adiaabat-1ph: A new public front-end to the MELTS,
1084 pMELTS, and pHMELTS models. *Geochemistry, Geophysics, Geosystems*, *6*(2), 1–8.
1085 <https://doi.org/10.1029/2004GC000816>
- 1086 Smythe, D. J., Wood, B. J., & Kiseeva, E. S. (2017). The S content of silicate melts at sulfide
1087 saturation: New experiments and a model incorporating the effects of sulfide composition.
1088 *American Mineralogist*, *102*(4), 795–803. <https://doi.org/10.2138/am-2017-5800CCBY>
- 1089 Spiegelman, M., Kelemen, P. B., & Aharonov, E. (2001). Causes and consequences of flow
1090 organization during melt transport: The reaction infiltration instability in compactible media.
1091 *Journal of Geophysical Research: Solid Earth*, *106*(B2), 2061–2077.
1092 <https://doi.org/10.1029/2000JB900240>

- 1093 Sun, W. (2007). Kinetics for coarsening co-controlled by diffusion and a reversible interface
1094 reaction. *Acta Materialia*, 55(1), 313–320. <https://doi.org/10.1016/j.actamat.2006.07.045>
- 1095 Sundberg, M., Hirth, G., & Kelemen, P. B. (2010). Trapped melt in the Josephine peridotite:
1096 Implications for permeability and melt extraction in the upper mantle. *Journal of Petrology*,
1097 51(1–2), 185–200. <https://doi.org/10.1093/petrology/egp089>
- 1098 Sweeney, S. M., & Martin, C. L. (2003). Pore size distributions calculated from 3-D images of
1099 DEM-simulated powder compacts. *Acta Materialia*, 51(12), 3635–3649.
1100 [https://doi.org/10.1016/S1359-6454\(03\)00183-6](https://doi.org/10.1016/S1359-6454(03)00183-6)
- 1101 von Bargen, N., & Waff, H. S. (1986). Permeabilities, interfacial areas and curvatures of partially
1102 molten systems: Results of numerical computations of equilibrium microstructures. *Journal of*
1103 *Geophysical Research*, 91(B9), 9261–9276. <https://doi.org/10.1029/JB091iB09p09261>
- 1104 Wagner, C. (1961). Theorie der Alterung von Niederschlägen durch Umlösen (Ostwald-
1105 Reifung). *Zeitschrift Für Elektrochemie, Berichte Der Bunsengesellschaft Für Physikalische*
1106 *Chemie*, 65(7–8), 581–591. <https://doi.org/10.1002/bbpc.19610650704>
- 1107 Wang, C., Liang, Y., Xu, W., & Dygert, N. (2013). Effect of melt composition on basalt and
1108 peridotite interaction: Laboratory dissolution experiments with applications to mineral
1109 compositional variations in mantle xenoliths from the North China Craton. *Contributions to*
1110 *Mineralogy and Petrology*, 166(5), 1469–1488. <https://doi.org/10.1007/s00410-013-0938-6>
- 1111 Wang, C., Liang, Y., Dygert, N., & Xu, W. (2016). Formation of orthopyroxenite by reaction
1112 between peridotite and hydrous basaltic melt: an experimental study. *Contributions to*
1113 *Mineralogy and Petrology*, 171(8–9). <https://doi.org/10.1007/s00410-016-1287-z>
- 1114 Wang, C., Lo Cascio, M., Liang, Y., & Xu, W. (2020). An experimental study of peridotite
1115 dissolution in eclogite-derived melts: Implications for styles of melt-rock interaction in
1116 lithospheric mantle beneath the North China Craton. *Geochimica et Cosmochimica Acta*, 278,
1117 157–176. <https://doi.org/10.1016/j.gca.2019.09.022>
- 1118 Wang, J., Xiong, X., Zhang, L., & Takahashi, E. (2020). Element loss to platinum capsules in
1119 high-temperature-pressure experiments. *American Mineralogist*, 105(10), 1593–1597.
1120 <https://doi.org/10.2138/am-2020-7580>
- 1121 Wang, K.-L., O'Reilly, S. Y., Griffin, W. L., Pearson, N. J., & Zhang, M. (2009). Sulfides in
1122 mantle peridotites from Penghu Islands, Taiwan: Melt percolation, PGE fractionation, and the

- 1123 lithospheric evolution of the South China block. *Geochimica et Cosmochimica Acta*, 73(15),
1124 4531–4557. <https://doi.org/10.1016/j.gca.2009.04.030>
- 1125 Wang, Z. J., & Jin, Z. (2020). Reaction Infiltration Instabilities in Partially Molten Peridotite and
1126 Implications for Driving the Transport of Sulfide Liquid. *Journal of Earth Science*, 31(3),
1127 447–455. <https://doi.org/10.1007/s12583-020-1301-2>
- 1128 Wang, Z. J., Jin, Z., Mungall, J. E., & Xiao, X. (2020). Transport of coexisting Ni-Cu sulfide
1129 liquid and silicate melt in partially molten peridotite. *Earth and Planetary Science Letters*,
1130 536, 116162. <https://doi.org/10.1016/j.epsl.2020.116162>
- 1131 Yao, Z. S., & Mungall, J. E. (2021). Kinetic controls on the sulfide mineralization of komatiite-
1132 associated Ni-Cu-(PGE) deposits. *Geochimica et Cosmochimica Acta*, 305, 185–211.
1133 <https://doi.org/10.1016/j.gca.2021.05.009>
- 1134 Yao, Z. S., Qin, K. Z., & Xue, S. C. (2017). Kinetic processes for plastic deformation of olivine
1135 in the Poyi ultramafic intrusion, NW China: Insights from the textural analysis of a ~ 1700 m
1136 fully cored succession. *Lithos*, 284–285, 462–476. <https://doi.org/10.1016/j.lithos.2017.05.002>
- 1137 Yao, Z. S., & Mungall, J. E. (2020). Flotation mechanism of sulphide melt on vapour bubbles in
1138 partially molten magmatic systems. *Earth and Planetary Science Letters*, 542, 116298.
1139 <https://doi.org/10.1016/j.epsl.2020.116298>
- 1140 Yao, Z. S., Qin, K. Z., & Mungall, J. E. (2018). Tectonic controls on Ni and Cu contents of
1141 primary mantle-derived magmas for the formation of magmatic sulfide deposits. *American*
1142 *Mineralogist*, 103(10), 1545–1567. <https://doi.org/10.2138/am-2018-6392>
- 1143 Yao, Z. S., Mungall, J. E., & Qin, K. Z. (2019). A preliminary model for the migration of sulfide
1144 droplets in a magmatic conduit and the significance of volatiles. *Journal of Petrology*, 60(12),
1145 2281–2316. <https://doi.org/10.1093/petrology/egaa005>
- 1146 Yao, Z. S., Mungall, J. E., & Jenkins, M. C. (2021). The Rustenburg Layered Suite formed as a
1147 stack of mush with transient magma chambers. *Nature Communications*, 12(1), 1–14.
1148 <https://doi.org/10.1038/s41467-020-20778-w>
- 1149 Yoshino, T., & Watson, E. B. (2005). Growth kinetics of FeS melt in partially molten peridotite:
1150 An analog for core-forming processes. *Earth and Planetary Science Letters*, 235(1–2), 453–
1151 468. <https://doi.org/10.1016/j.epsl.2005.04.021>
- 1152 Yoshino, T., Walter, M. J., & Katsura, T. (2003). Core formation in planetesimals triggered by
1153 permeable flow. *Nature*, 422(6928), 154–157. <https://doi.org/10.1038/nature01459>

- 1154 Yoshino, T., Walter, M. J., & Katsura, T. (2004). Connectivity of molten Fe alloy in peridotite
1155 based on in situ electrical conductivity measurements: Implications for core formation in
1156 terrestrial planets. *Earth and Planetary Science Letters*, 222(2), 625–643.
1157 <https://doi.org/10.1016/j.epsl.2004.03.010>
- 1158 Yoshino, T., Laumonier, M., McIsaac, E., & Katsura, T. (2010). Electrical conductivity of
1159 basaltic and carbonatite melt-bearing peridotites at high pressures: Implications for melt
1160 distribution and melt fraction in the upper mantle. *Earth and Planetary Science Letters*,
1161 295(3–4), 593–602. <https://doi.org/10.1016/j.epsl.2010.04.050>
- 1162 Zhang, Y. (2015). Toward a quantitative model for the formation of gravitational magmatic
1163 sulfide deposits. *Chemical Geology*, 391, 56–73.
1164 <https://doi.org/10.1016/j.chemgeo.2014.10.025>
- 1165 Zhang, Y., Walker, D., & Leshner, C. E. (1989). Diffusive crystal dissolution. *Contributions to*
1166 *Mineralogy and Petrology*, 102(4), 492–513. <https://doi.org/10.1007/BF00371090>
- 1167 Zhang, Y., Ni, H., & Chen, Y. (2010). Diffusion data in silicate melts. *Reviews in Mineralogy*
1168 *and Geochemistry*, 72(1), 311–408. <https://doi.org/10.2138/rmg.2010.72.8>
- 1169 Zhao, Y., Liu, S. A., Xue, C., & Li, M. L. (2022). Copper isotope evidence for a Cu-rich mantle
1170 source of the world-class Jinchuan magmatic Ni-Cu deposit. *American Mineralogist*, 107(4),
1171 673–683. <https://doi.org/10.2138/am-2021-7911>
- 1172 Zhu, W., Gaetani, G. A., Füsseis, F., Montési, L. G. J., & de Carlo, F. (2011). Microtomography
1173 of partially molten rocks: Three-dimensional melt distribution in mantle peridotite. *Science*,
1174 332(6025), 88–91. <https://doi.org/10.1126/science.1202221>
- 1175

1176 **Figure 1.** Back-scattered electron images (BSE) of sections from experiments PC520 (a)
1177 (annealing time ~ 12 h) and PC545 (b) (annealing time ~ 72 h) under the conditions of 1.5 GPa
1178 and 1,250 °C. Dashed red and blue lines respectively denote the original and current interfaces
1179 between the melt source and peridotite before and after the melt-rock reaction. The dashed
1180 yellow line marks the top of the Opx-rich reaction layer. The position where the melt fraction at
1181 the top of the melt source decreases below 10 – 15 vol% is set as the possible lower boundary of
1182 ORL for the measurement (the dashed white line), which is approximately consistent with the
1183 original interface between the melt source and peridotite at short annealing time (< 48 h). The
1184 width of these quenched cracks needs to be subtracted. The specimen setup of these experiments

1185 is shown as the inset in the left lower part. Mineral abbreviations: Ol-olivine; Opx-
1186 orthopyroxene; SM-silicate melt; SL-sulfide liquid.

1187 **Figure 2.** Microstructures of the interface of melt-rock reaction in experiments PC545 (72 h,
1188 1,250 °C) (a), PC528 (48 h, 1,250 °C) (b, c), and PC527 (12 h, 1,300 °C) (d). Detailed
1189 microstructure of the distribution of sulfide droplets and silicate melt in the partially molten
1190 peridotite is displayed in (c). Symbols are the same as in Figure 1. Mineral abbreviations: Ol-
1191 olivine; Opx-orthopyroxene; SM-silicate melt; SL-sulfide liquid. Note that some huge Opx
1192 grains are present in the Opx-rich reaction layer of experiment PC527 with high reaction
1193 temperature, potentially leading to the destruction of the layer.

1194 **Figure 3.** Plots of thicknesses of Opx-rich reaction layers (ORL) (a) and dissolution distance (b)
1195 as a function of the square root of run time. The lines show the best fit for these data. k is the
1196 diffusive dissolution or growth rate which is the slope of the linear regression line. The grey
1197 symbols and lines denoted as 3 and 4 are from Morgan & Liang (2005), and those denoted as 1,
1198 2, 5, and 6 are from C. Wang et al. (2020). The blue symbols and lines denoted as 7 are from this
1199 study. Note that the dissolution distance and the thickness of ORL may be slightly
1200 underestimated and overestimated, respectively, due to the possible gravitational settling of
1201 minerals in our experiments.

1202 **Figure 4.** Plots of melt fraction (a) and grain size of silicate minerals (b) as a function of the
1203 square root of run time in the partially molten peridotite from our experiments.

1204 **Figure 5.** Plots of grain size (μm) of sulfide droplets weighted by the area (a and c) and the area
1205 fraction of sulfide droplets (b and d) as a function of the square root of run time in the melt
1206 source (lower part) and partially molten peridotite (upper part). Inset in (a) shows the
1207 relationship between the number density of sulfide droplets in the melt source and the square
1208 root of run time. All symbols representing samples are the same as those in (c).

1209 **Figure 6.** Plots (a-g) of measured oxide abundance (in wt.%) and Mg# in olivine as a function of
1210 distance (in μm) away from the melt-rock interface. The compositional variations of MgO, Mg#,
1211 and FeO are also simulated thermodynamically as a function of the melt-peridotite ratio in (h).
1212 These measured compositions of olivine approaching to the interface are roughly consistent with

1213 those results simulated thermodynamically (the gray shadow region in h), when the melt-rock
1214 ratio ranges from 1 to 1.5 (Table S6). At low pressure (PC559, 0.5 GPa), the compositions of
1215 olivine recrystallized in the melt source during the melt-rock reaction are present as PC559-
1216 Lower (hollow black square). The compositions of olivine grains within the low-temperature
1217 hot-press experiment (PC537) were almost constant across the partially molten peridotite region
1218 and thus can be used as the reference line (purple dotted lines) to show the composition
1219 variations of olivine in those high-temperature reaction experiments. The gray shadow regions in
1220 (a)-(g) denote the region that has a vigorous melt-peridotite reaction, whose width is not in
1221 accordance with the actual distance.

1222 **Figure 7.** Plots (a-g) of oxide abundance (in wt.%) and Mg# in clinopyroxene as a function of
1223 distance (in μm) away from the melt-rock interface. The compositional variations of MgO,
1224 Al_2O_3 , and CaO are also simulated thermodynamically as a function of the melt-peridotite ratio
1225 in (h). The legends are the same as in Figure 6.

1226 **Figure 8.** Plots of oxide abundance (in wt.%) (a-e), sulfur content (f), and viscosity (μ_m) (g) of
1227 silicate melt versus the run time in melt-rock interface and lower melt source of these reaction
1228 experiments. The ranges of composition variations of SiO_2 , Al_2O_3 , FeO, CaO, and MgO
1229 simulated thermodynamically are denoted as shadow gray regions in (a)-(e) when the melt-
1230 peridotite ratio varies from 1 to 1.5. The shadow gray region in (f) is the calculated SCSS based
1231 on the models from Chowdhury & Dasgupta (2020) and Smythe et al. (2017), and the SCSS
1232 value at $t = 0$ is calculated by using the compositions of starting materials under conditions of
1233 1,250 °C and 1.5 GPa. The composition of sulfides in starting materials (Table S3) was used to
1234 estimate the SCSS in experiments PC559 and PC560. Produced phase proportions of different
1235 silicate minerals during the melt-rock reaction are simulated thermodynamically as a function of
1236 melt-peridotite ratio in (h). A lower melt viscosity ($\sim 0.25 \text{ Pa}\cdot\text{s}$) of the carbonate-bearing
1237 experiment (PC560) is roughly estimated by using a model from Di Genova et al. (2014)
1238 considering the effect of CO_3^{2-} ($\sim 2 \text{ wt.}\%$) and denoted as a hollow inverted triangle in (g). Cpx-
1239 clinopyroxene, Opx-orthopyroxene.

1240 **Figure 9.** Normalized 3D size distributions of sulfide droplets in melt source. The size of sulfide
1241 droplets (r) and frequency (f) have been normalized to average size (r^*) and maximum frequency
1242 (f_{max}), respectively.

1243 **Figure 10.** Schematic map illustrating the fluid flow around a circular cylindrical particle
1244 confined by two parallel flat plates (a), the dimensionless coefficients f_D is shown as a function
1245 of the R/r_s ratio (b) (modified from Lee & Fung, 1969), and the extrusion and entrainment of
1246 large (left side) and small (right side) sulfide droplets driven by focused melt flow (c). In (a), the
1247 two parallel flat plates and a circular cylindrical particle are considered as the walls of the pore
1248 throat/melt channel and sulfide droplet, respectively.

1249 **Figure 11.** Plots of the radius (r_s) of initial undeformed sulfide droplets that could extrude the
1250 pore throat as a function of the porosity (Φ) of the partially molten mantle. The relationship
1251 between r_s and Φ is divided into three parts according to the relative size of sulfide droplets'
1252 radius (r_s) and the pore throat's minimum constriction (R). The description of these three regions
1253 can be found in the main text.

1254 **Table 1.** Experimental conditions and the observed lithologies.

Figure 1.

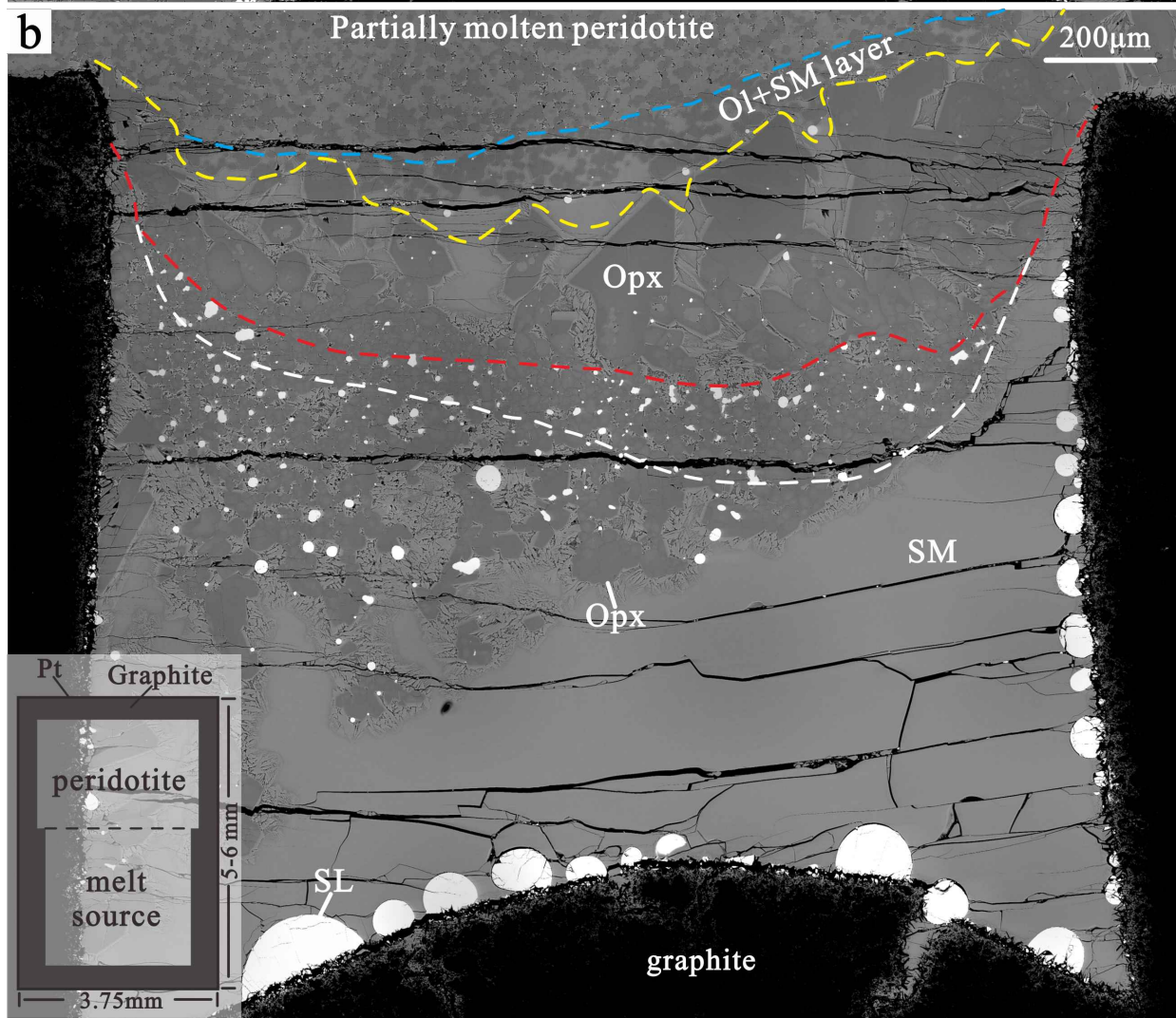
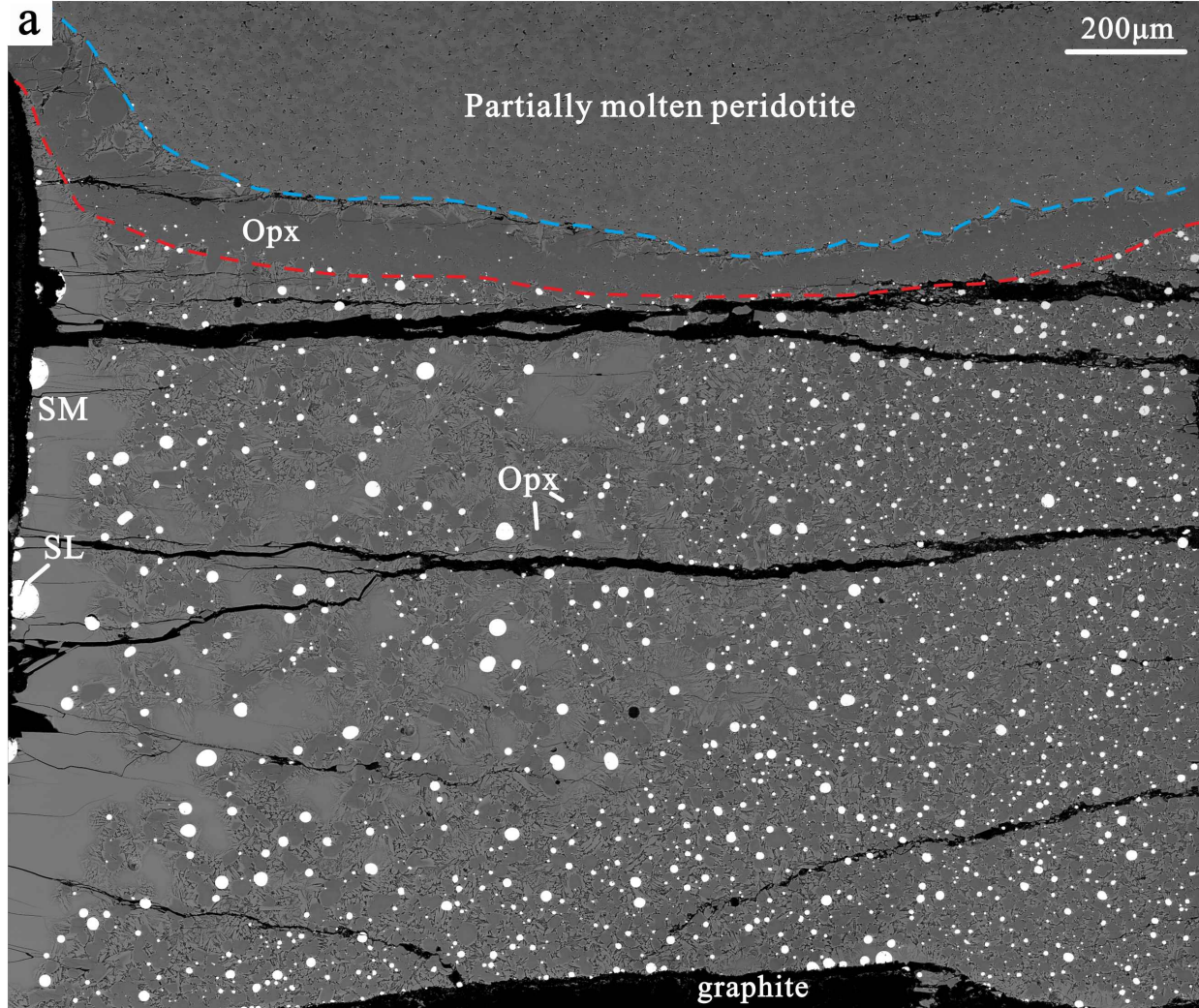


Figure 2.

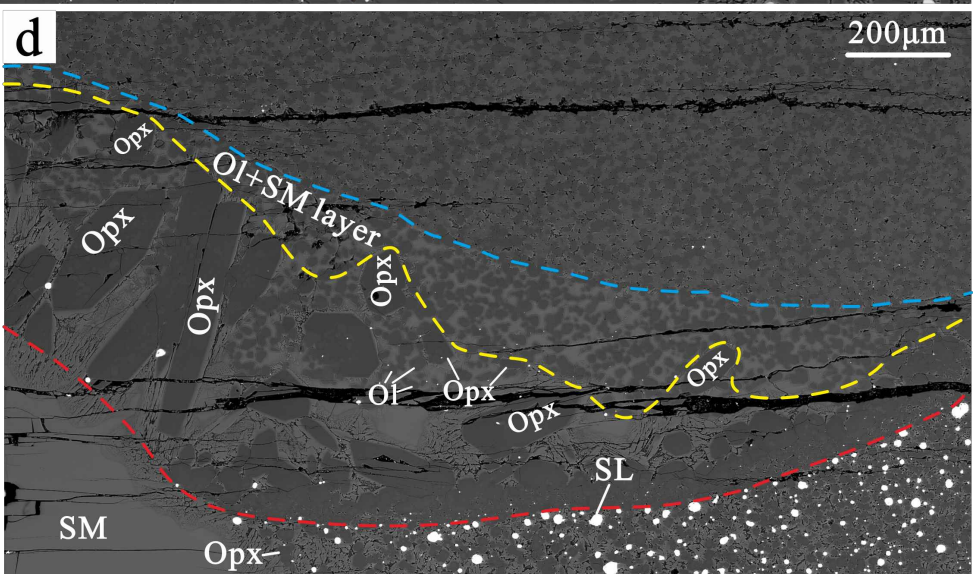
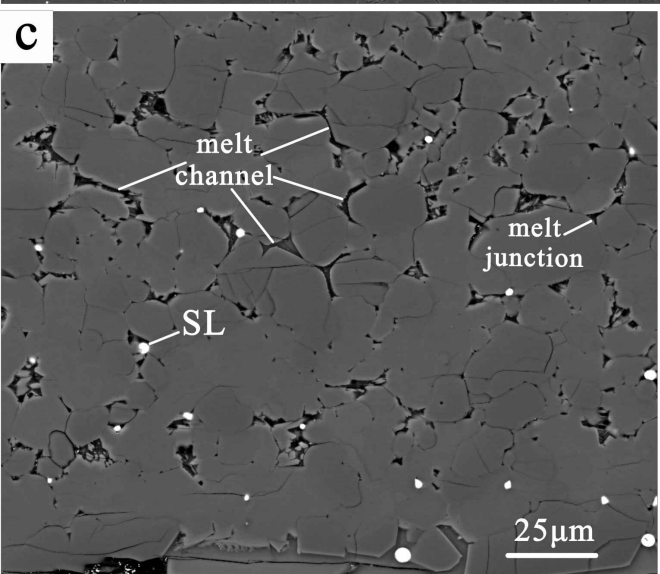
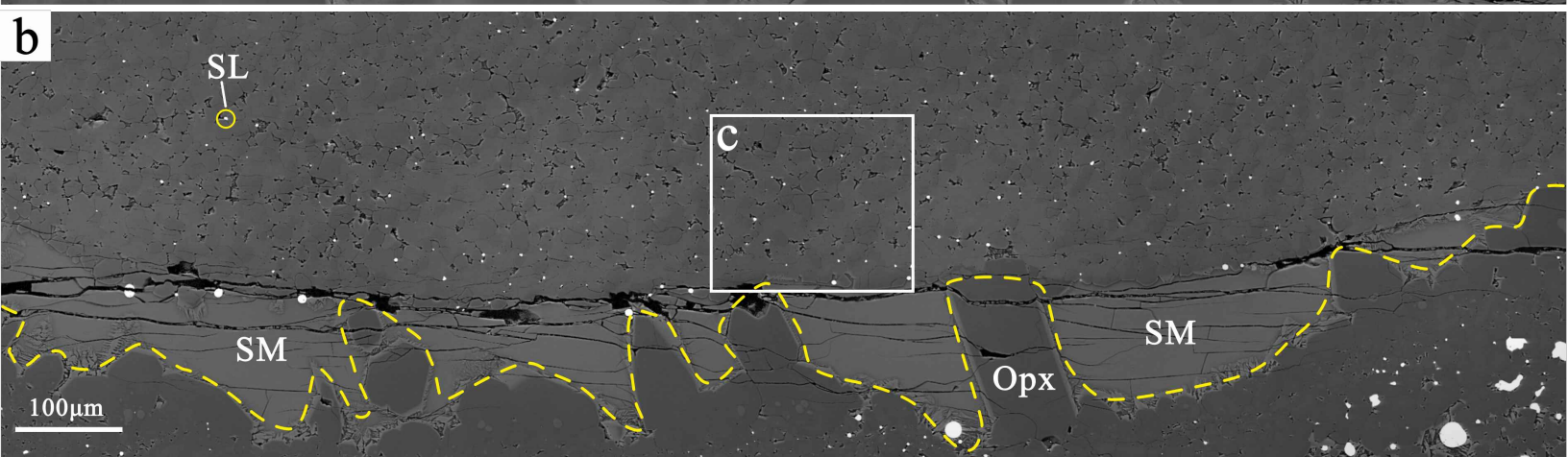
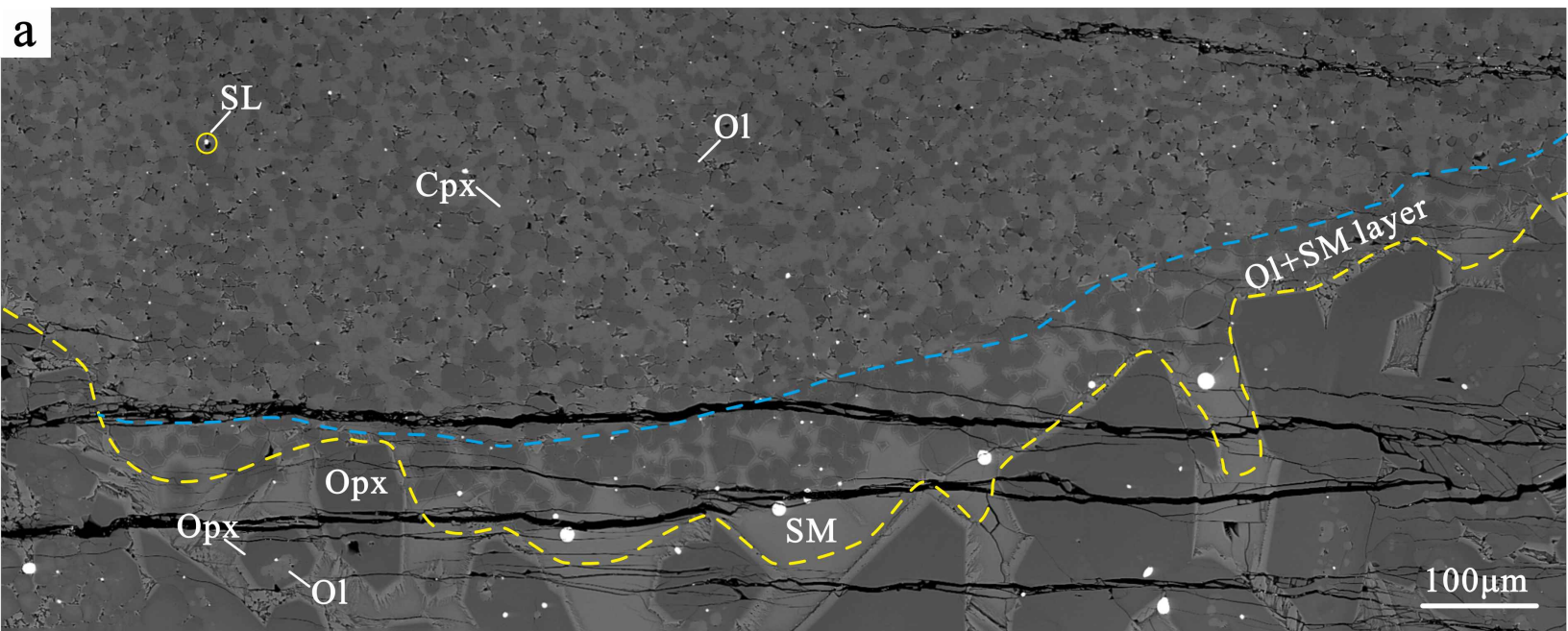


Figure 3.

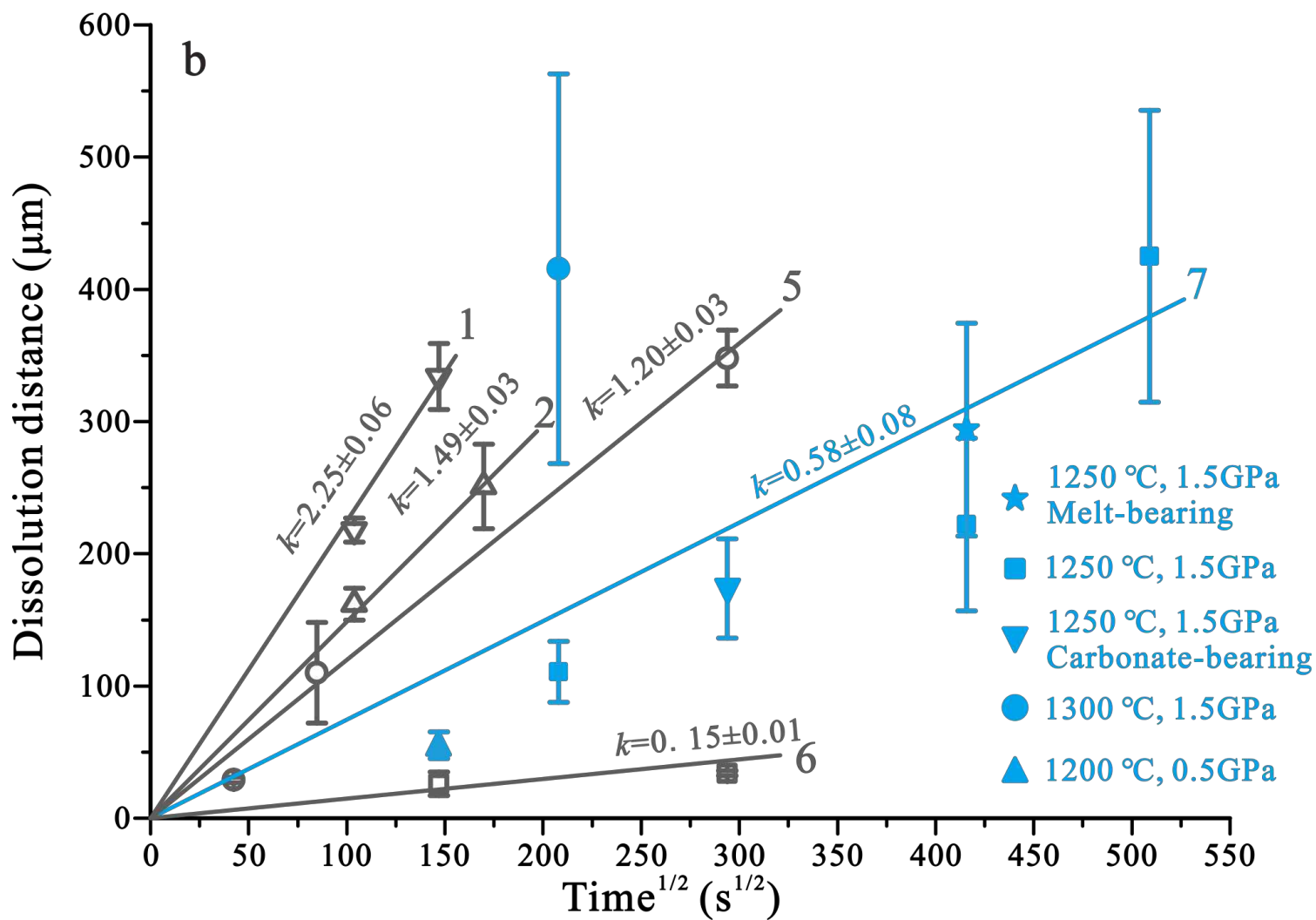
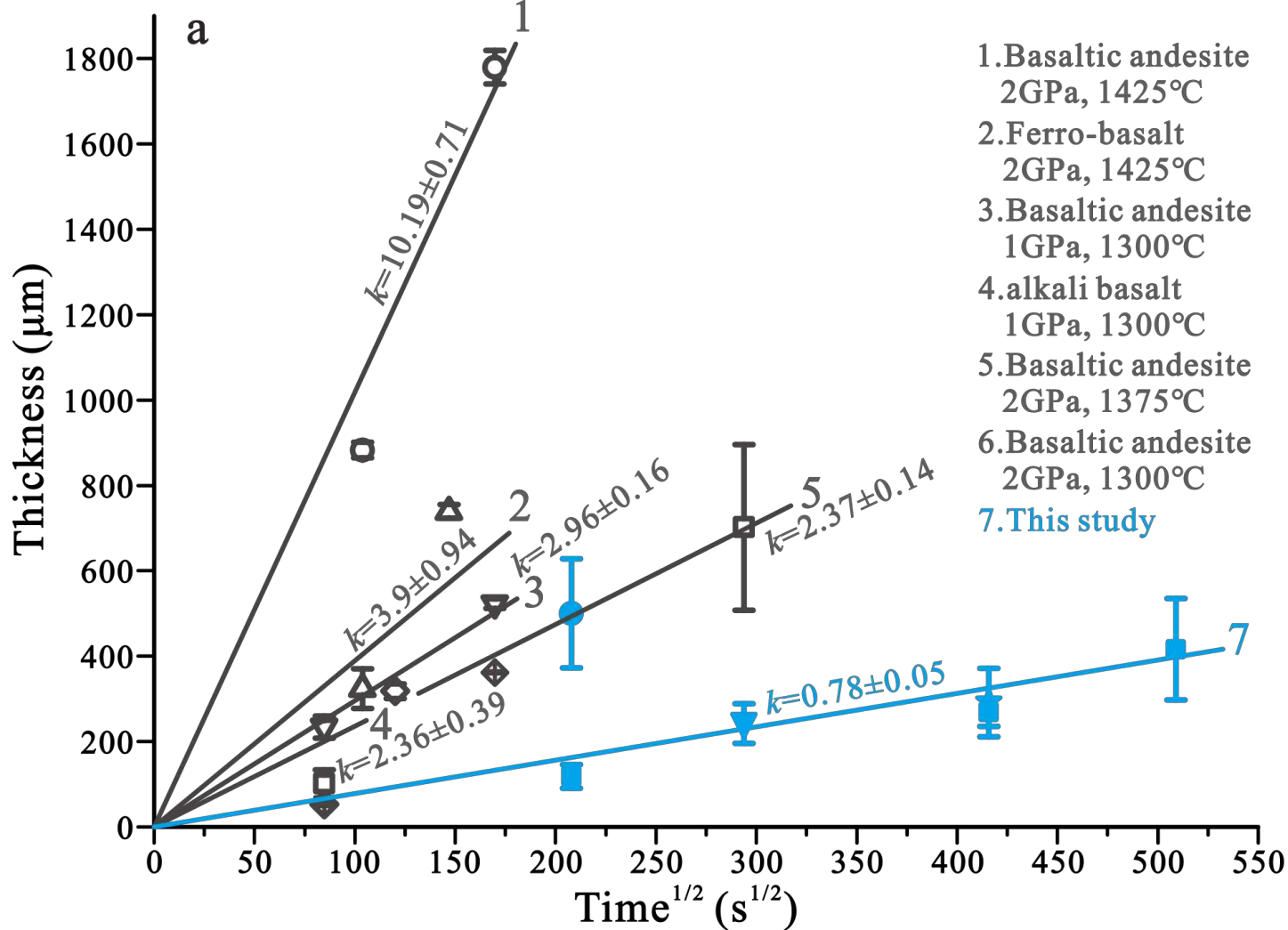


Figure 4.

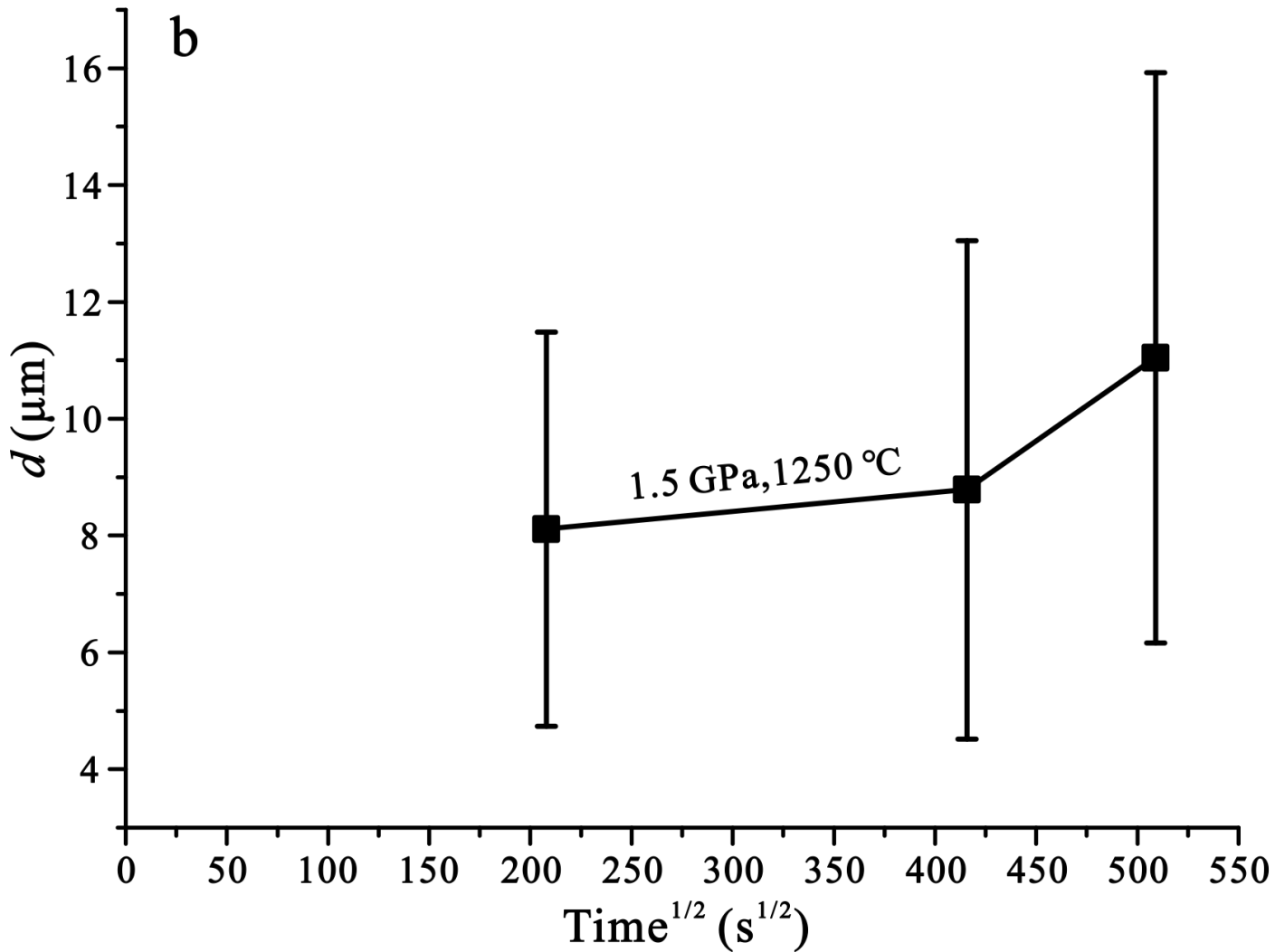
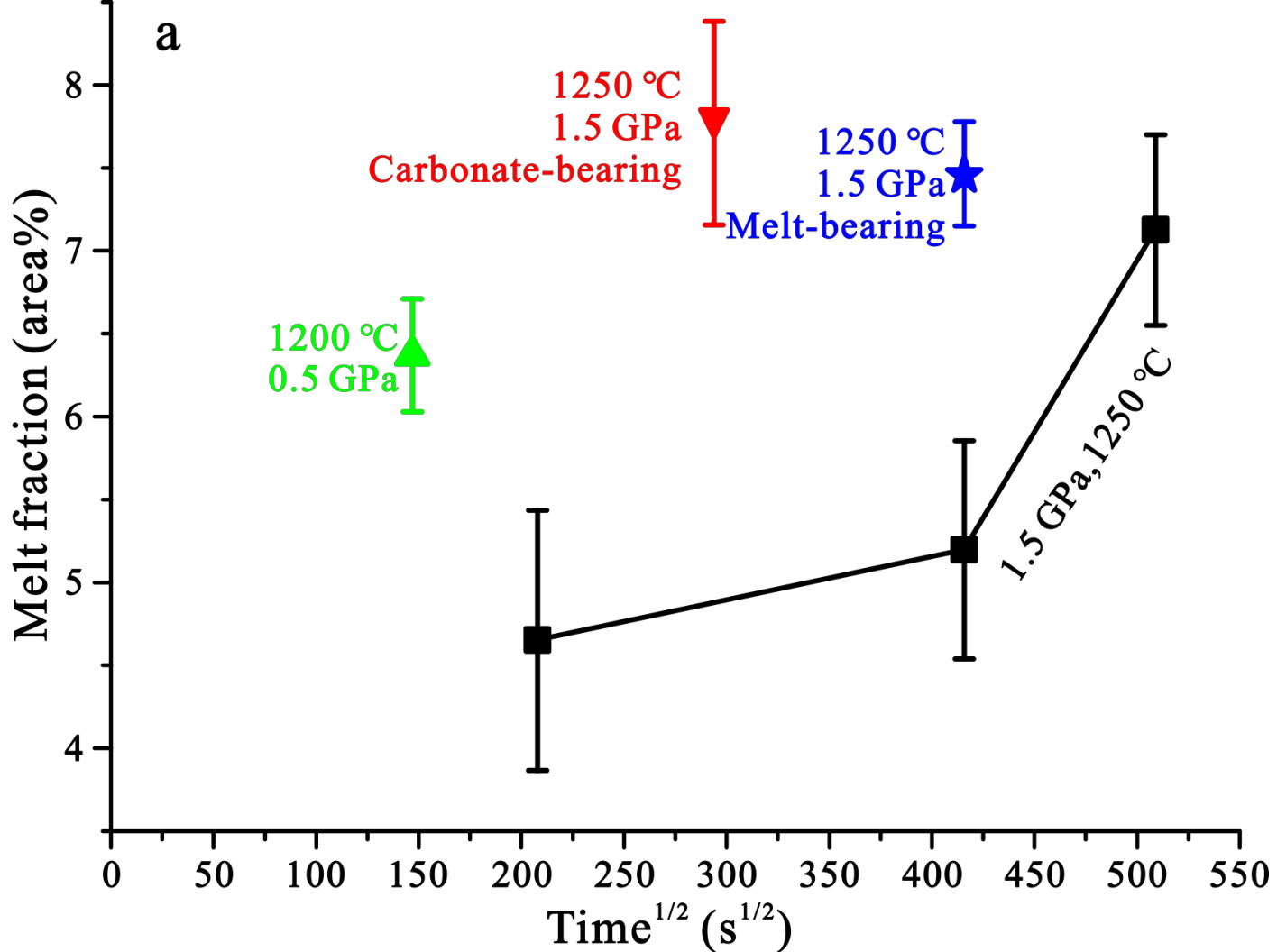


Figure 5.

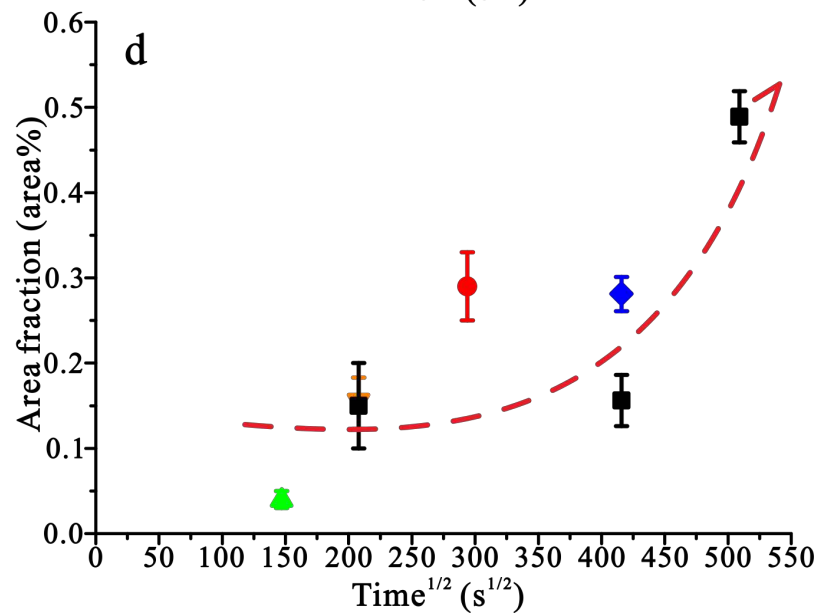
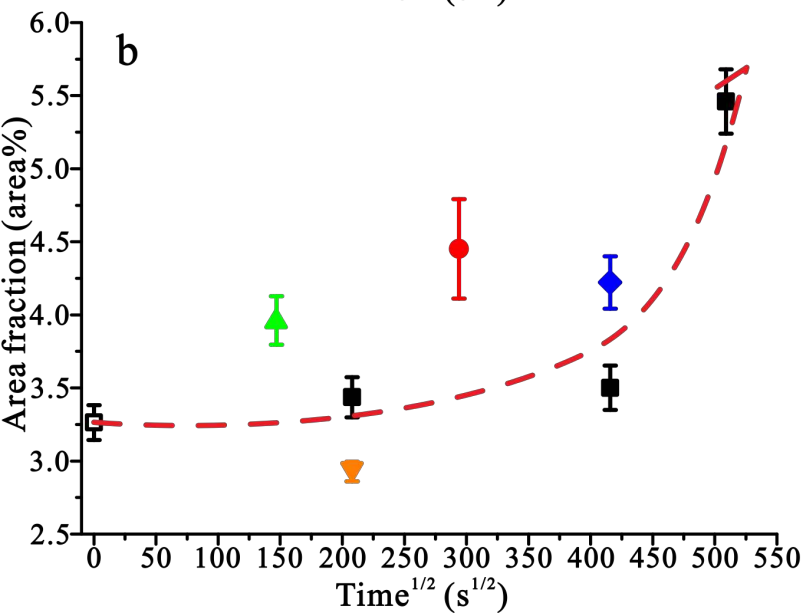
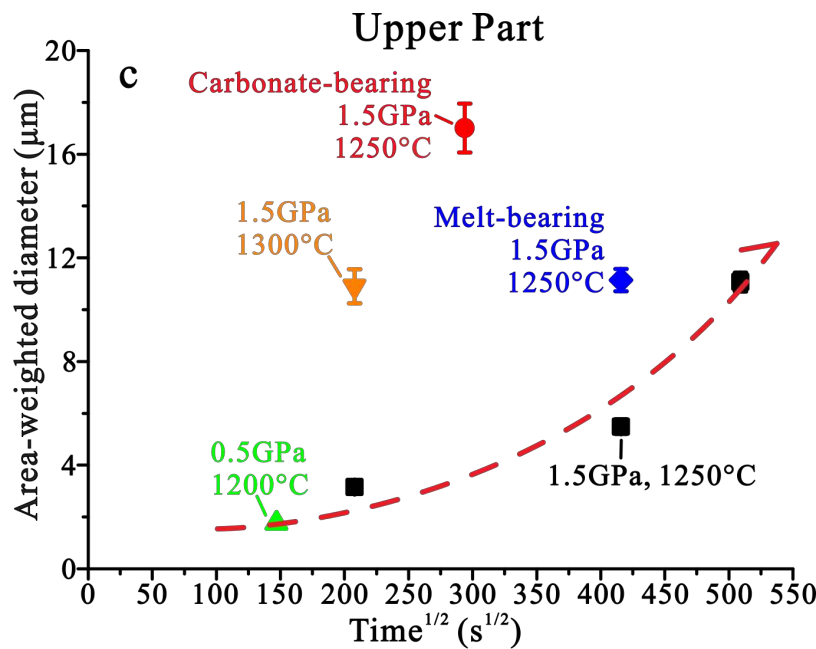
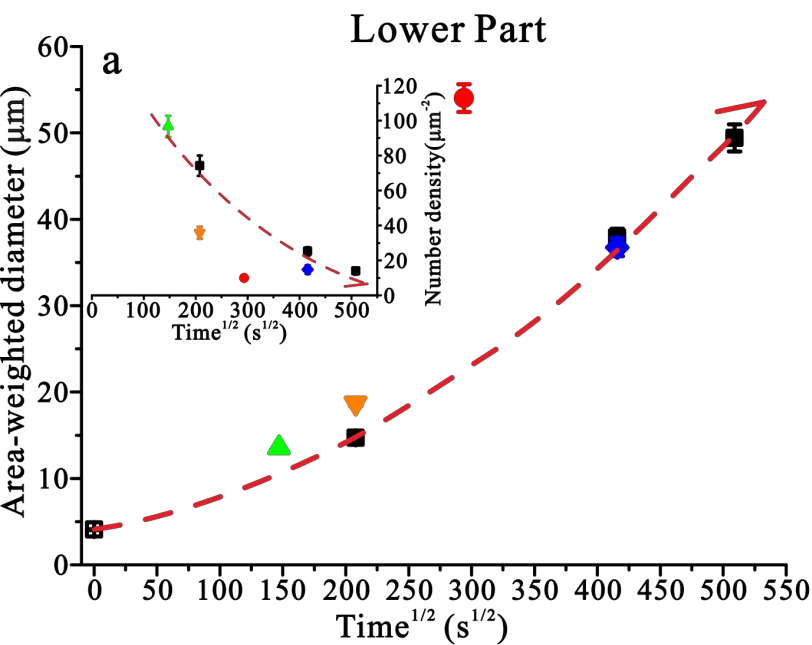


Figure 6.

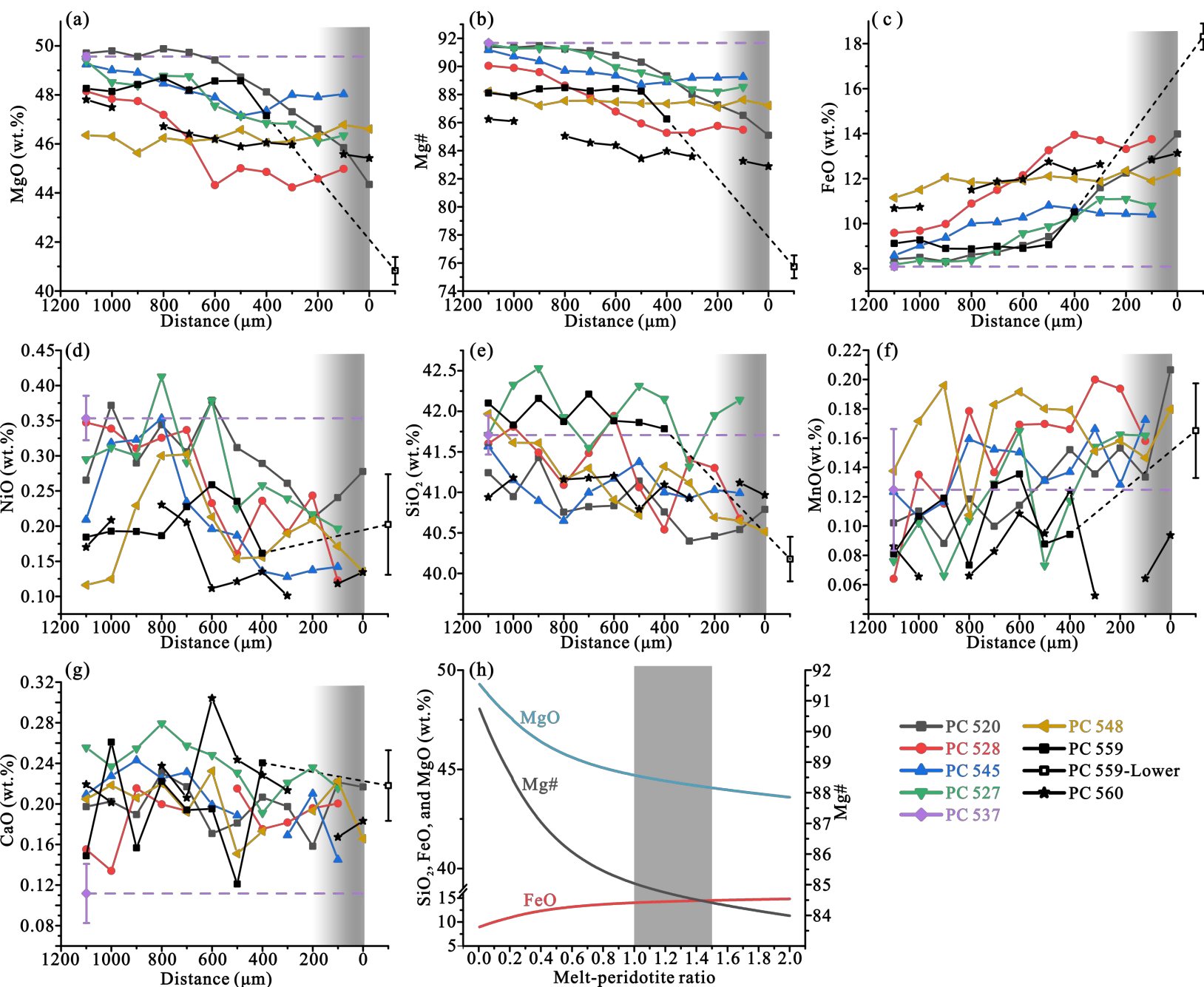


Figure 7.

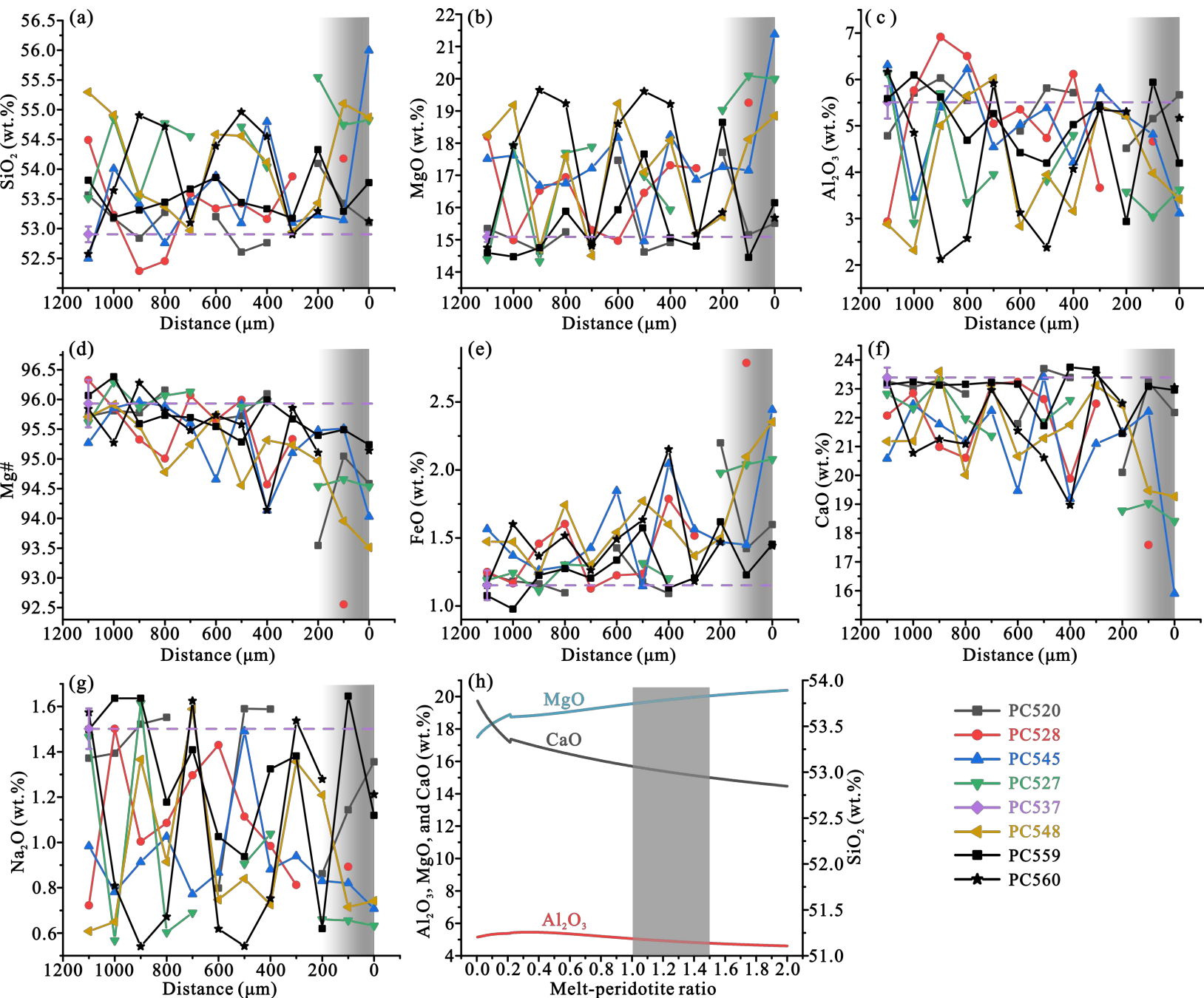


Figure 8.

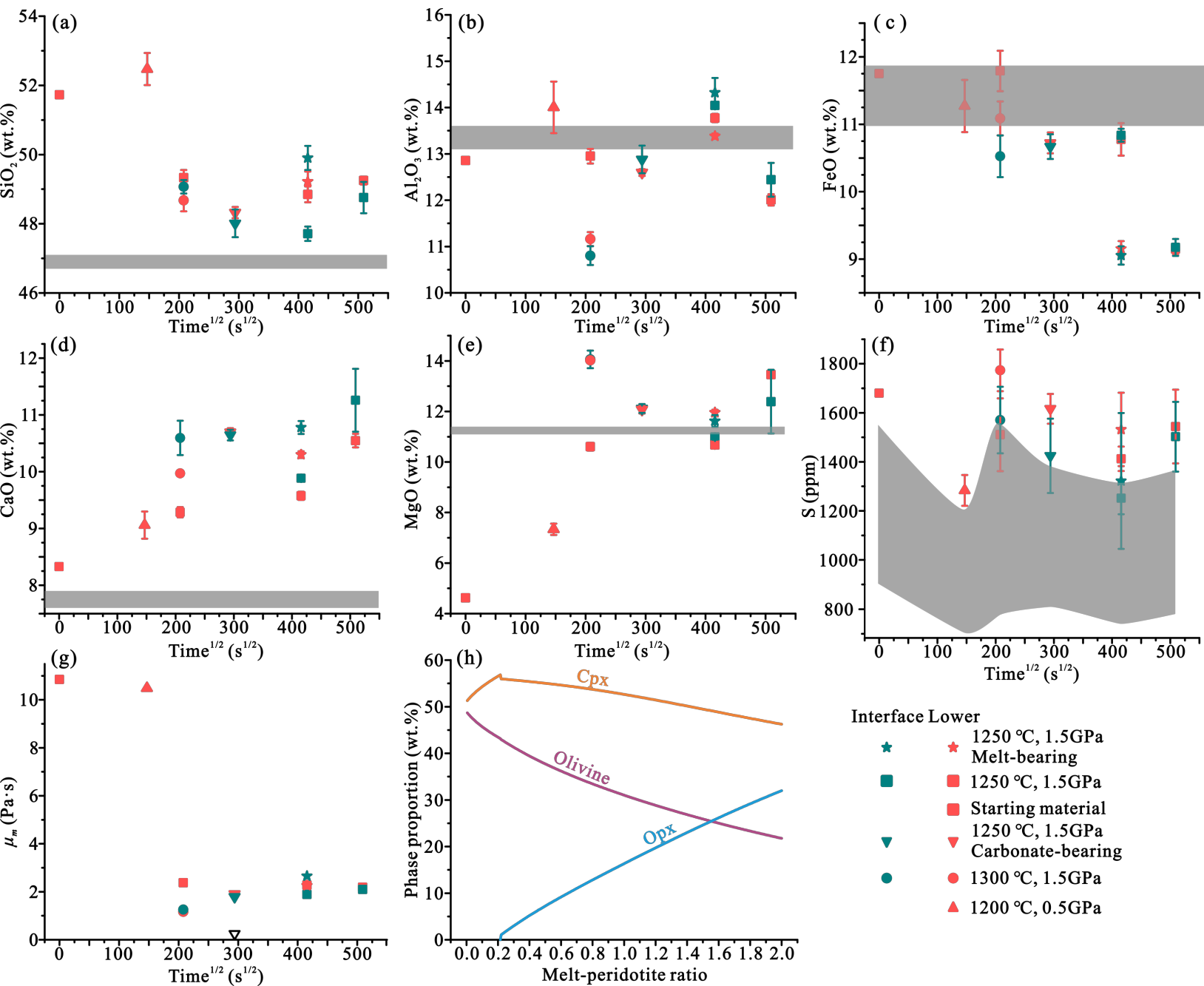


Figure 9.

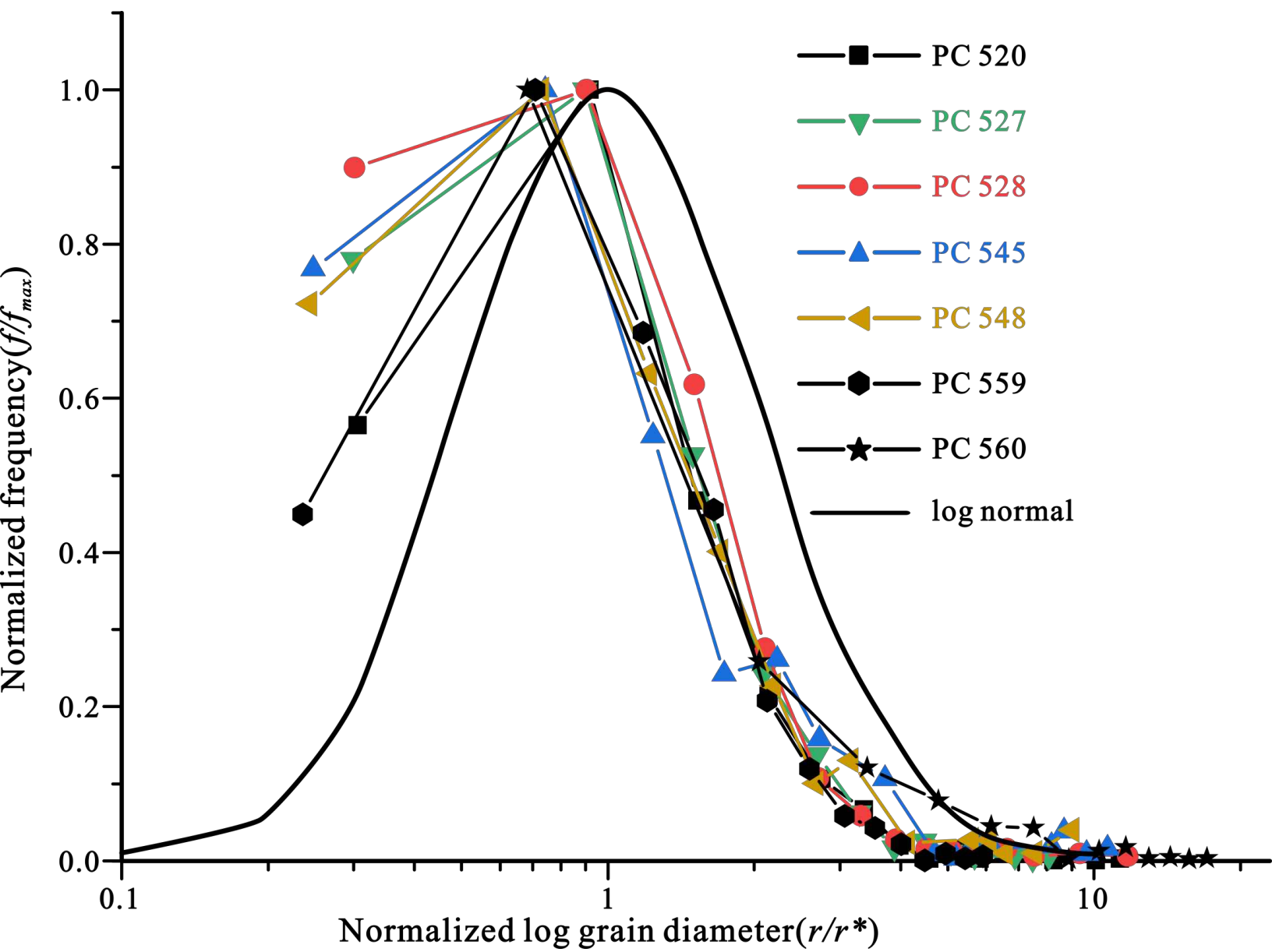


Figure 10.

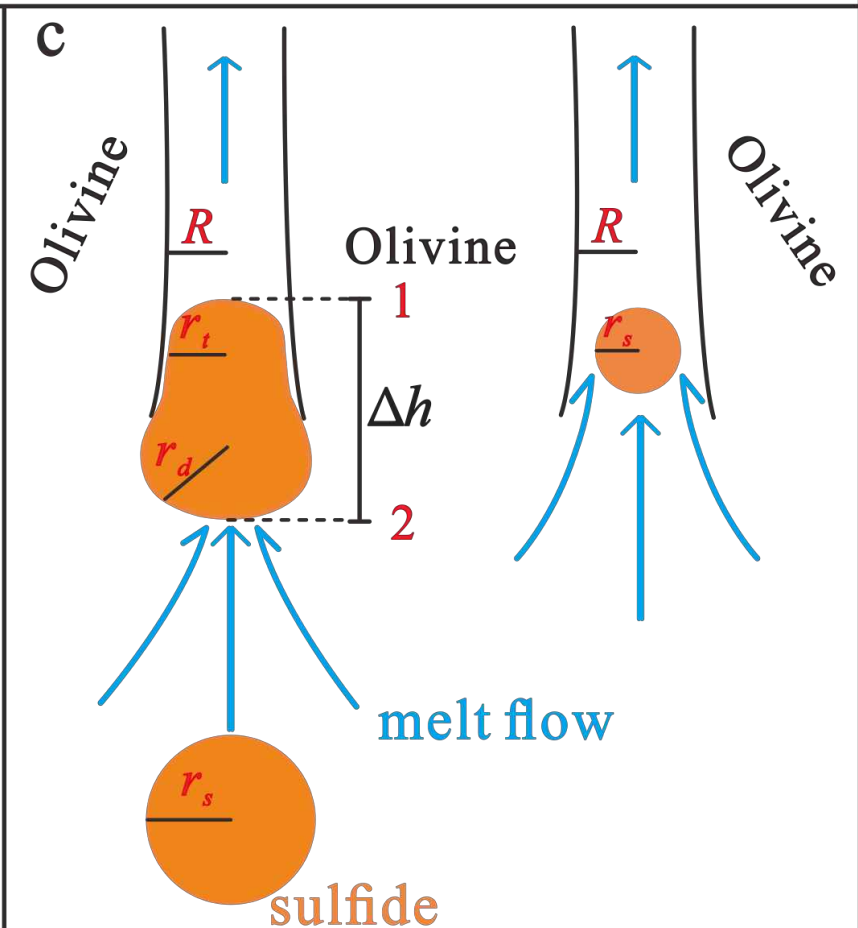
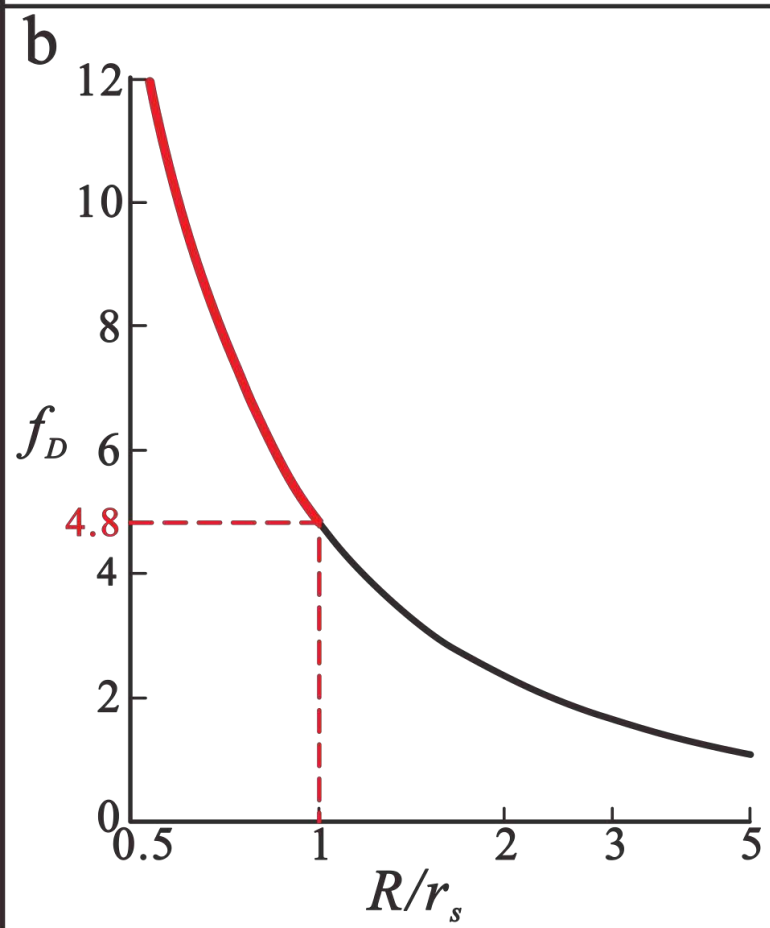
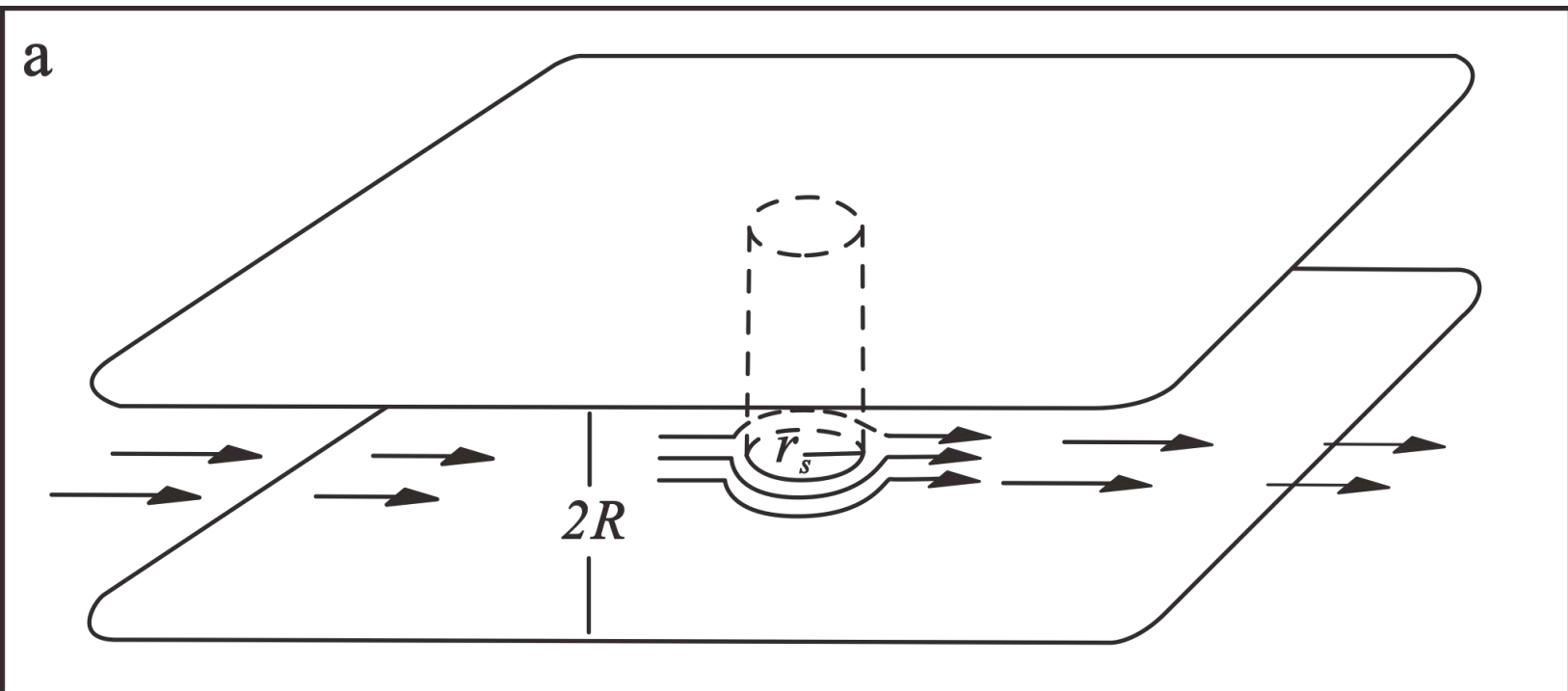


Figure 11.

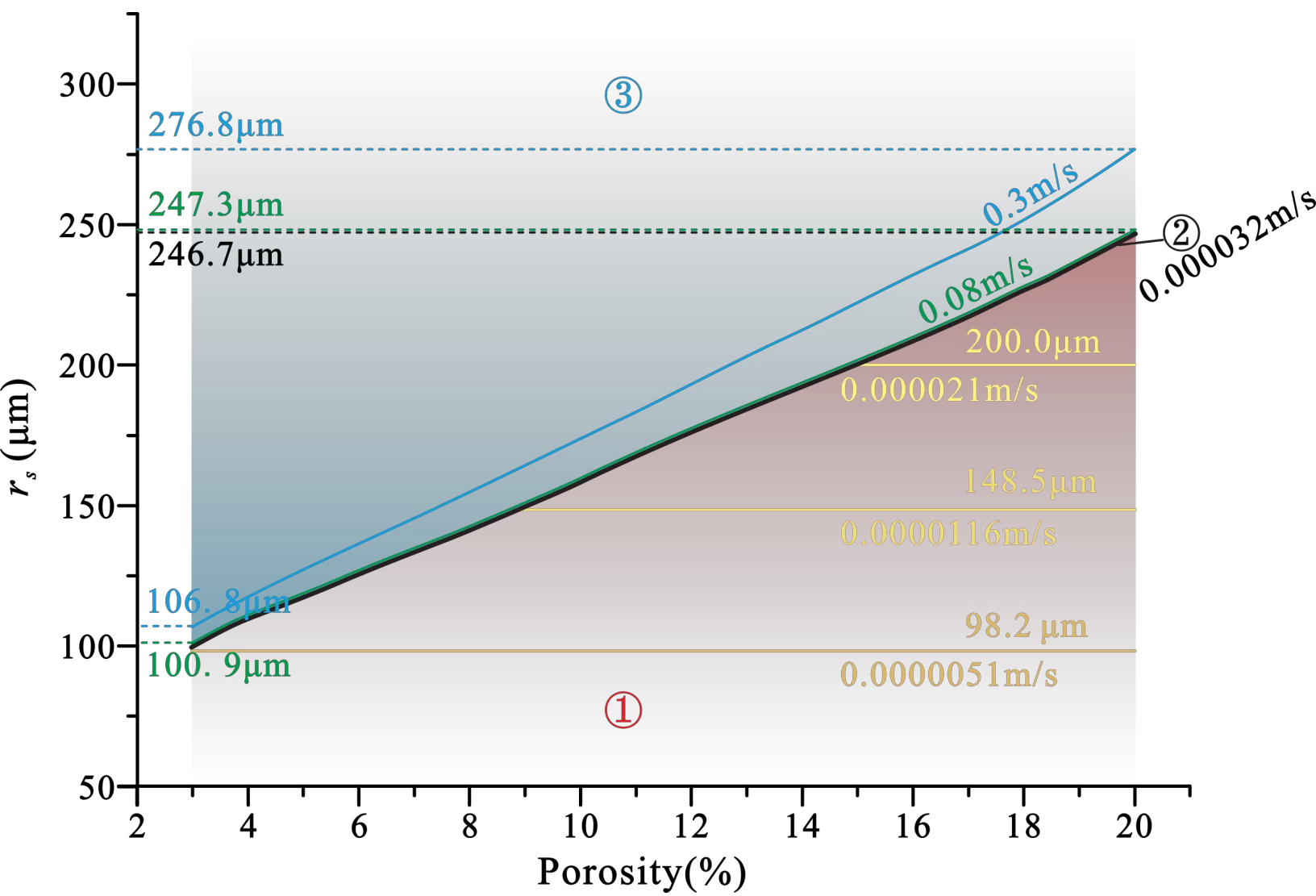


Table 1. Experimental conditions and the observed lithologies

NO.	Starting material (upper peridotite/lower melt source)	Experimental conditions (P/GPa, T/°C, t/h)	Capsule	Lithologies (upper peridotite/reaction interface/melt source)
PC520		1.5, 1250, 12		Ol+Cpx+SM+SL/ ORL/ Opx+SM+SL
PC527		1.5, 1300, 12		Ol+Cpx+SM+SL/ Ol-SM layer/ ORL/ Opx+SM+SL
PC528	Ol+Cpx/ Ol+basalt+sulfide	1.5, 1250, 48		Ol+Cpx+SM+SL/ ORL/ Opx+SM+SL
PC537		1.5, 800, 12		Ol+Cpx/ Ol+basalt+sulfide
PC545		1.5, 1250, 72	Pt-graphite	Ol+Cpx+SM+SL/ Ol-SM layer/ ORL/ Opx+SM+SL
PC548	Ol+Cpx+basalt (5wt.%)/ Ol+basalt+sulfide	1.5, 1250, 48		Ol+Cpx+SM+SL/ ORL/ Opx+SM+SL
PC559		0.5, 1200, 6		Ol+Cpx+SM+SL+V/ Ol+SM+SL
PC560	Ol+Cpx+basalt (5wt.%)/ Ol+basalt+carbonate (2wt.%)+sulfide	1.5, 1250, 24		Ol+Cpx+SM+SL/ Ol-SM layer/ ORL/ Opx+SM+SL

Note: Ol-olivine; Cpx-clinopyroxene; SM-silicate melt; SL-sulfide liquid; V-vapor bubble; ORL-orthopyroxene-rich reaction layer.